

Textural, Compositional, and Sulfur Isotope Variations of Sulfide Minerals in the Red Dog Zn-Pb-Ag Deposits, Brooks Range, Alaska: Implications for Ore Formation

K. D. KELLEY,[†] D. L. LEACH,

U.S. Geological Survey, Box 25046, MS 973, Denver, Colorado 80225

C. A. JOHNSON,

U.S. Geological Survey, Box 25046, MS 963, Denver, Colorado 80225

J. L. CLARK,

Teck Cominco American Inc., 15918 East Euclid Avenue, Spokane, Washington 99216

M. FAYEK,

Oak Ridge National Laboratories, P.O. Box 2008, Oak Ridge, Tennessee 37831

J. F. SLACK,

U.S. Geological Survey, National Center, MS 954, Reston, Virginia 20192

V. M. ANDERSON,

1175 C Bear Mountain Drive, Boulder, Colorado 80305

R. A. AYUSO,

U.S. Geological Survey, National Center, MS 954, Reston, Virginia 20192

AND W. I. RIDLEY

U.S. Geological Survey, Box 25046, MS 973, Denver, Colorado 80225

Abstract

The Red Dog Zn-Pb deposits are hosted in organic-rich mudstone and shale of the Mississippian Kuna Formation. A complex mineralization history is defined by four sphalerite types or stages: (1) early brown sphalerite, (2) yellow-brown sphalerite, (3) red-brown sphalerite, and (4) late tan sphalerite. Stages 2 and 3 constitute the main ore-forming event and are volumetrically the most important. Sulfides in stages 1 and 2 were deposited with barite, whereas stage 3 largely replaces barite. Distinct chemical differences exist among the different stages of sphalerite. From early brown sphalerite to later yellow-brown sphalerite and red-brown sphalerite, Fe and Co content generally increase and Mn and Tl content generally decrease. Early brown sphalerite contains no more than 1.9 wt percent Fe and 63 ppm Co, with high Mn (up to 37 ppm) and Tl (126 ppm), whereas yellow-brown sphalerite and red-brown sphalerite contain high Fe (up to 7.3 wt %) and Co (up to 382 ppm), and low Mn (<27 ppm) and Tl (<37 ppm). Late tan sphalerite has distinctly lower Fe (<0.9 wt %) and higher Tl (up to 355 ppm), Mn (up to 177 ppm), and Ge (426 ppm), relative to earlier sphalerite. Wide ranges in concentrations of Ag, Cu, Pb, and Sb characterize all sphalerite types, particularly yellow-brown sphalerite and red-brown sphalerite, and most likely reflect submicroscopic inclusions of galena, chalcopyrite and/or tetrahedrite in the sphalerite. In situ ion microprobe sulfur isotope analyses show a progression from extremely low $\delta^{34}\text{S}$ values for stage 1 (as low as -37.2‰) to much higher values for yellow-brown sphalerite (mean of 3.3‰ ; $n = 30$) and red-brown sphalerite (mean of 3.4 ; $n = 20$). Late tan sphalerite is isotopically light (-16.4 to -27.2‰).

The textural, chemical, and isotopic data indicate the following paragenesis: (1) deposition of early brown sphalerite with abundant barite, minor pyrite, and trace galena immediately beneath the sea floor in unconsolidated mud; (2) deposition of yellow-brown sphalerite during subsea-floor hydrothermal recrystallization and coarsening of preexisting barite; (3) open-space deposition of barite, red-brown sphalerite and other sulfides in veins and coeval replacement of barite; and (4) postore sulfide deposition, including the formation of late tan sphalerite breccias. Stage 1 mineralization took place in a low-temperature environment where fluids rich in Ba mixed with pore water or water-column sulfate to form barite, and metals combined with H_2S derived from bacterial sulfate reduction to form sulfides. Higher temperatures and salinities and relatively oxidized ore-stage fluids (stages 2 and 3) compared with stage 1 were probably important controls on

[†]Corresponding author: e-mail, kdkelley@usgs.gov

the abundances and relative amounts of metals in the fluids and the resulting sulfide chemistry. Textural observations and isotopic data show that preexisting barite was reductively dissolved, providing a source of H_2S for sulfide mineral formation. In stage 3, the continued flow of hydrothermal fluids caused thermal alteration of organic-rich mudstones and a build-up of methane that led to fluid overpressuring, hydrofracturing, and vein formation. Barite, red-brown sphalerite, and other sulfides were deposited in the veins, and preexisting barite was pervasively replaced by red-brown sphalerite. Hydrothermal activity ceased until Jurassic time when thrusting and large-scale fluid flow related to the Brookian orogeny remobilized and formed late tan sphalerite in tectonic breccias.

Introduction

THE RED DOG district, which includes four primary deposits at Red Dog (Qanaiyaq, Main, Aqqaluk, and Paalaaq), as well as the Anarraaq, Su-Lik, and numerous other smaller deposits (Fig. 1), contains one of the world's largest reserves and resources of zinc totaling 140.6 Mt with an average of 16.6 percent Zn and 4.6 percent Pb (Jennings and King, 2002). To date, all of the production in the district has come from the Main deposit open pit mine, which is operated by Teck Cominco Alaska under an agreement with the Northwest Alaska

Native Association. Throughout this paper, the term "Red Dog deposits" refers collectively to the Qanaiyaq, Main, Aqqaluk, and Paalaaq deposits. The term "Red Dog district" comprises the four Red Dog deposits as well as the Anarraaq, Su-Lik, and other smaller deposits in the area.

The paragenesis, mineral textures, and compositional variations of sulfides in the Red Dog deposits have been determined from samples collected from surface exposures and/or drill core (Fig. 1), providing important insights into the geochemical processes and geologic controls responsible for mineralization. Textural variations provide constraints on the processes by which minerals formed within the host rocks. Variation in trace element abundances in hydrothermal sulfides through the paragenesis is a sensitive indicator of changes in the chemistry of ore-forming fluids. And, sulfur isotope compositions of the sulfides and associated sulfates constrain the origin of sulfur in the deposits.

The mineralogy of the Red Dog deposits is a simple assemblage of barite, sphalerite, galena, pyrite, and marcasite. The textures of the ores are varied, however, and paragenetic studies underscore a complex history of mineralization. Recent advancements in analytical techniques now allow for in situ microanalysis of sulfide minerals, thereby preserving the paragenetic and textural context of the analyses. Laser ablation-inductively coupled plasma-mass spectrometry (LA-ICP-MS) was used for direct trace element analysis of sulfide minerals. The LA-ICP-MS method is a powerful tool that has been applied to analyses of a wide range of trace metals in minerals (Ridley and Lichte, 1998; Ridley, 2000), and recent development of appropriate sulfide standards for calibration (Wilson et al., 2002) has enhanced the applicability of the method to sulfides in particular. Secondary ionization mass spectrometry (SIMS) was used for measurement of $^{34}S/^{32}S$ ratios; advancements in this method have allowed for in situ analyses with high spatial resolution (10–50 μm) and precision and reproducibility at the ± 0.5 per mil (2σ) level (e.g., McKibben and Ricuputi, 1998).

This paper presents an interpretation of the mineral textures in the Red Dog deposits and a discussion of the chemical and isotopic variations of the sulfides. These data are used to interpret the depositional environment and refine genetic models for the Red Dog deposits. Only the Red Dog deposits are included in this study; similar studies at Anarraaq and other deposits in the district are ongoing.

Analytical Methods

LA-ICP-MS

LA-ICP-MS was performed on sulfide minerals in standard polished thin sections using laboratory facilities at the U.S. Geological Survey in Denver, Colorado. An ultraviolet laser source was used to heat and ablate surface particles from the solid mineral that are then transported in a stream of argon

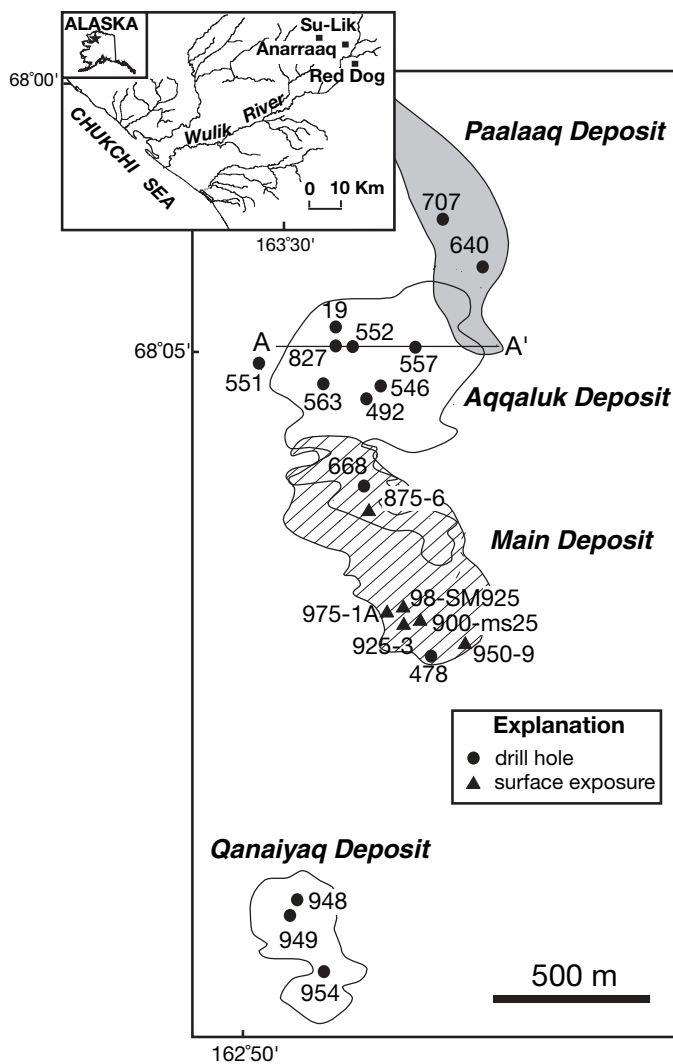


FIG. 1. Map showing the four deposits at Red Dog with locations of samples collected from surface exposures and drill holes. Cross section A-A' across the Aqqaluk deposit is shown in Figure 3. Inset shows relationship of the Red Dog deposits to other deposits in the district.

gas to an inductively coupled argon plasma where they are vaporized, dissociated, and ionized. The ions, dominated by singly charged species, are extracted from the plasma and separated according to their mass-to-charge ratio using a quadrupole mass spectrometer.

A spot size of 50 μm was chosen for the analyses and used for all sulfide minerals to provide consistency in the data. Although care was taken to choose analytical points free of surficial mineral inclusions, the depth of penetration of the laser beam (ca. 5–10 μm) makes the incorporation of small inclusions possible. However, the software program used to reduce the data allows the user to include only specific portions of the total spectra generated by the analyses; therefore, those parts of the spectra that were obviously produced by submicroscopic inclusions were identified and excluded during data reduction. The results of the analyses were calibrated using either a glass or a synthetic sulfide standard developed by Wilson et al. (2002). Precision of the technique is about 2 to 8 percent (Ridley, 2000; Norman et al., 2003). Details of the method and detection limits are included in Ridley and Lichte (1998) and Ridley (2000).

Prior to LA-ICP-MS analysis, many samples were independently analyzed for major and minor elements using the electron microprobe (EMP). This allowed a determination of the level of heterogeneity of the samples and provided a crosscheck on some of the elements analyzed by the LA-ICP-MS method.

Secondary ionization mass spectrometry

Sulfur isotope compositions of pyrite, galena, and sphalerite were measured in situ using a CAMECA ims 4f ion microprobe at Oak Ridge National Laboratories in Oak Ridge, Tennessee. The analytical protocol for S isotope measurements is similar to that described by Riciputi (1996). Sulfur isotope ratios ($^{34}\text{S}/^{32}\text{S}$) from sulfides were measured using a Cs^+ primary beam. A normal-incidence flood gun was employed to neutralize potential sample charging. The primary ion beam was focused to a $15 \times 30 \mu\text{m}$ spot using a $100 \mu\text{m}$ aperture in the primary column. Secondary sulfur ions were detected sequentially by switching the magnetic field. The detection system (Balzers electron multiplier) was coupled with an ion counting system with an overall dead time of 8.5 ns. A typical analysis lasts ~12 min, comprising 100 analysis cycles (Riciputi et al., 1998).

During the isotope measurement by ion microprobe, an intrinsic mass dependent bias (referred to as instrumental mass fractionation) is introduced. A variety of processes combine to produce this fractionation, including secondary atom extraction (sputtering) and ionization (e.g., Williams, 1979; Yu and Lang, 1986) and secondary ion transmission (Shimizu and Hart, 1982; Valley and Graham, 1991). The greatest contributors to instrumental mass fractionation are sputtering and ionization, which depend most strongly on sample composition, referred to as compositionally dependent fractionations or matrix effects (e.g., Valley et al., 1997). Correction for this mass fractionation is done by comparing measurements of a chemically and isotopically homogeneous mineral standard that is chemically similar to the unknown sample. Ion microprobe results for the standard are compared with its accepted isotopic composition in order to compute a correction factor that is applied to the unknowns measured during the same analysis session (e.g., Leshin et al., 1998). Standards used in

this study are Balmat sphalerite (14.0‰ CDT), Balmat pyrite (14.6‰ CDT), and Balmat galena (15.6‰ CDT) from the Balmat mine, New York (Crowe and Vaughan, 1996).

The precision and accuracy of analyses include errors arising from counting statistics, calibration to a known standard, and uncertainty in dead-time corrections owing to variable count rates. In general, the overall analytical precision for the sulfides is ± 0.8 per mil. Values are reported in standard notation relative to Cañon Diablo Troilite (CDT).

Geology of the Red Dog Deposits

Basin setting and age

The Red Dog Zn-Pb-Ag strata-bound massive sulfide bodies are hosted by black shale and mudstone of the Mississippian Kuna Formation. Subduction during the Jurassic to Cretaceous Brookian orogeny resulted in a complex structural setting consisting of multiple, fault-bounded and age-equivalent allochthons (Mull, 1982; Mayfield et al., 1988). In the southern Brooks Range, the rocks were metamorphosed to blueschist and greenschist facies (informally called the schist belt), whereas in the north (foothills of the Brooks Range where Red Dog is located) they are primarily folded unmetamorphosed to weakly metamorphosed sedimentary rocks (Moore et al., 1994). Paleogeographic reconstructions suggest that mineralization occurred along a passive continental margin in a Carboniferous basin containing calcareous turbidite, mudstone, and shale of the Kuna Formation (Dumoulin et al., 2004; Young, 2004) and overlying conglomerates and sandstones of Late Devonian to Early Mississippian age. Volumetrically minor alkali basalts and felsic volcanic and intrusive rocks in the Kuna Formation are present both regionally and locally in the Red Dog area (Moore et al., 1986; Werdon, 1996). The entire succession of Upper Devonian-Carboniferous sedimentary strata (clastic rocks and overlying shale-carbonate sequence) in the Red Dog area is less than 1 km thick (Young, 2004), but about 200 km to the east the sedimentary package is nearly 4 km thick (Mull and Werdon, 1994).

The ore deposits are restricted to the uppermost unit, informally named the Ikalukrok unit, of the Kuna Formation (Mull et al., 1982). The upper Ikalukrok, which hosts the deposits, is late Meramecian to early Chesterian in age (about 340 to 330 Ma; Harland et al., 1990) on the basis of conodonts and radiolarians (Dumoulin et al., 2004). The age of Red Dog ore is constrained by Re-Os dating of hydrothermal pyrite, which yields an isochron age of 338 ± 5.8 Ma (Morelli et al., 2004). The Ikalukrok unit, which is 30 to 240 m thick in the district (Dumoulin et al., 2004), consists of finely laminated, black, siliceous and carbonaceous shale and mudstone with locally abundant carbonate turbidites. Deposition of the Kuna Formation took place in a basin and slope setting characterized by anoxic or dysaerobic bottom waters and by high productivity of organic matter possibly related to local upwelling (Slack et al., 2004a). The locally abundant calcareous turbidite layers (2 cm to >4 m thick) were derived by erosion of carbonate platforms that flanked the basin (Dumoulin et al., 2004). On the basis of the presence of minor alkali basalts and regional Carboniferous tectonic relationships, the basin is inferred to have been of extensional origin (Young, 2004). Deposition of the upper Kuna Formation during late

Meramecian time coincided with very sharp reductions in sedimentation rates owing to the drowning of adjacent platforms and the end of carbonate deposition in the basin (Dumoulin et al., 2004). Rifting and tectonic subsidence and flooding of cold upwelling currents from the Kuna basin onto adjacent carbonate platforms may have been factors in the demise of these platforms (Dumoulin et al., 2004).

Ore deposit stratigraphy and zoning

All sulfide ore is hosted by Ikalukrok shale and mudstone of the uppermost Kuna Formation (Figs. 2 and 3). Base-metal

sulfide minerals are present in only minor amounts in the underlying calcareous shale (informally named the Kivalina unit). All four Red Dog deposits have similar ore assemblages, degree of silicification, and host-rock lithology, but some of the primary characteristics have been obscured by postmineralization deformation during the Jurassic to Cretaceous Brookian orogeny. The deposits are structurally separated, and the Qanaiyaq, Main, Aqqaluk, and Paalaaq orebodies lie in distinct thrust panels within an overall duplex structure (Jennings and King, 2002). The result is a series of stacked orebodies, in which each deposit lies at successively

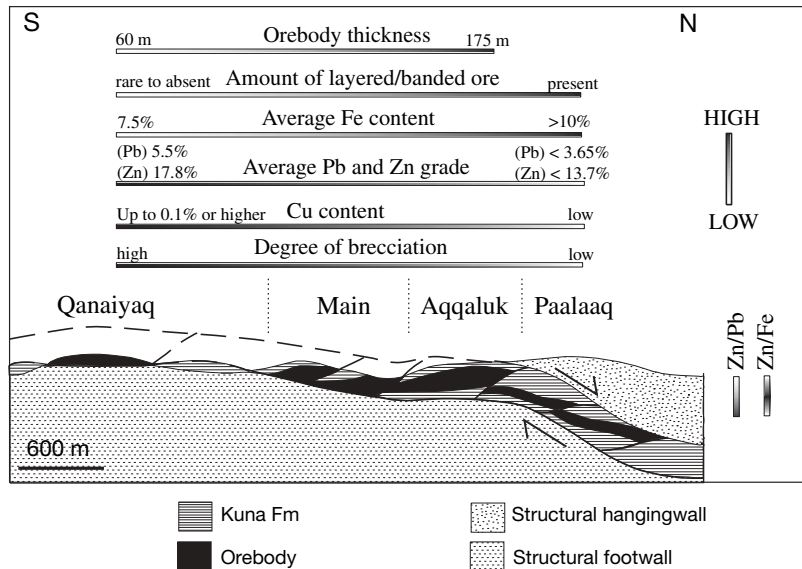


FIG. 2. Long section from Qanaiyaq to Paalaaq showing deepening from south to north owing to Brookian thrusting (modified from Jennings and King, 2002). Also shown are horizontal and vertical geochemical and textural trends.

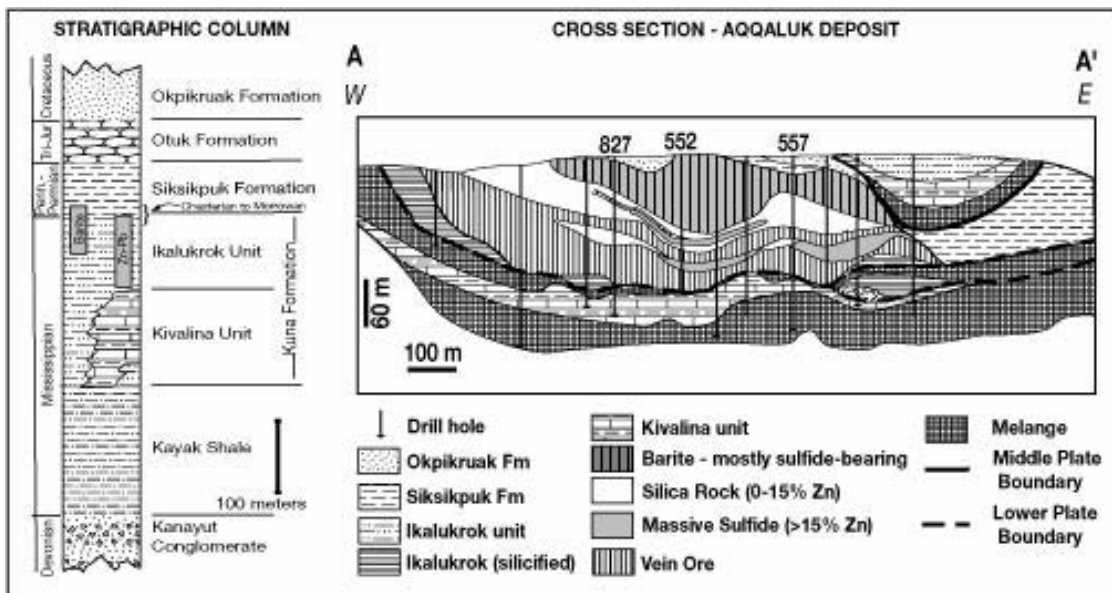


FIG. 3. Generalized stratigraphic column (modified from Young, 2004) and cross section across the Aqqaluk deposit. Note the stratigraphic position of the orebody and typical thickness of barite and Zn-Pb mineralized zones. Okpikruak Formation comprises micaceous sandstone and mudstone, Otuk and Siksikpuk Formations comprise dominantly chert and shale, Ikalukrok unit comprises shale and mudstone with interbedded carbonate, Kivalina unit comprises calcareous shale, Kayak Shale comprises sandstone, shale, and limestone, and Kanayut Conglomerate comprises conglomerate, sandstone and minor shale.

greater depths from south to north (Fig. 2). The degree of deformation and faulting, particularly in the Main and Paalaaq deposits, makes reconstruction of the original deposit configuration difficult. However, Aqqaluk displays a relatively continuous, less structurally disrupted section compared with the other deposits.

From the top down, the ore deposits are characterized by (1) sulfide-poor barite, (2) sulfide-bearing barite, (3) silica rock or silicified barite, (4) massive sulfide, and (5) sulfide-veins of the Ikalukrok unit (Fig. 3). These ore types have been thoroughly described by Moore et al. (1986) and Sims (1996) and are only briefly discussed here. Sulfide-poor barite is present at the top of each deposit at the contact between the Ikalukrok unit and the Siksikuk Formation, which occupies a stratigraphic position of Chesterian to Morrowan (Late Mississippian to Early Pennsylvanian), on the basis of conodont and radiolarian ages in the Red Dog area (Dumoulin et al., 2004). Sulfide-poor barite is white to light gray, fine-grained, and commonly well bedded (Moore et al., 1986). Sulfide-bearing barite is characterized by two distinct textural types: white to gray, fine-grained (10–50 μm) equigranular grains intergrown with sulfides, and white, coarse-grained (up to 3 cm) crystals with interstitial sulfides. Although rare, iron or other base-metal sulfides crudely interlayered with barite are locally present, particularly in the Aqqaluk and Paalaaq deposits.

The term silica rock is applied to strongly silicified barite (Sims, 1996; Leach et al., 2004); it consists of a white to translucent gray rock composed of mostly medium-grained, zoned euhedral quartz. Massive sulfide (Fig. 3) has greater than 40 wt percent sulfide minerals and includes both semi-massive and massive sulfide ore as described by Moore et al. (1986) and Young (1989). Rare banded sulfides in shale have been observed, mainly at Aqqaluk and Paalaaq. Most of the ore is massive and unbedded, consisting of abundant sulfide grains and aggregates disseminated in a dense silica matrix. Fragmental textures also are present in massive sulfide ore.

Although sulfide veins are present in all of the deposits, they are most abundant and consistently developed at Aqqaluk, where they are found at the base and periphery and less commonly in the center of the deposit. The veins typically cut silicified black shale of the Ikalukrok unit, silica rock, and massive sulfide ore but are absent in sulfide-bearing barite. The veins are steeply dipping, trend north-northeast (Moore et al., 1986), and vary in width from 1 mm to one meter. Vein density can be high enough to constitute bulk ore grade zones. Coarse, angular, sulfide-cemented breccias related to the main mineralizing system are particularly well developed near areas of intense veining, but they also are present throughout the deposits (Moore et al., 1986).

Other breccias consist of very fine grained, light-tan sphalerite and silica enclosing angular fragments of host rocks and clasts of vein sulfide. These breccias have not been described previously at Red Dog, but they cut all rock types and hence formed late in the history of the deposits. The breccia bodies or masses generally display shallow dips consistent with dips of thrust faults in the region and contrasting with the steeply dipping veins.

Proportions of the total tonnage contributed by the different ore types are estimated from mine statistics for the Main

deposit. About 20 percent of the tonnage being mined is from sulfide-bearing barite, 58 percent is from massive sulfide, and 21 percent is from vein ore (T. Krolak, writ. commun., 2002). Similar percentages are calculated from resources and reserves at Aqqaluk.

Although all four deposits display a similar sequence of ore types from top to bottom, differences exist in orebody thickness, proportion of ore types and styles, and average grade from south to north (Fig. 2). Estimates of prethrusting thicknesses of combined barite and sulfides suggest that Qanaiyaq is thinner than Aqqaluk (Edgerton, 1997), which in turn is thicker than Paalaaq (T. Krolak, writ. commun., 2002). Qanaiyaq is approximately 60 m thick, the Main deposit is 90 to 120 m thick, and Aqqaluk (Fig. 3) is 175 m thick. Paalaaq has not been extensively drilled, but estimates suggest the original thickness was 20 to 30 m, although some intervals may have been 100 m thick.

In addition to thickness variations, there are differences in the proportions of ore types. The amount of brecciation decreases and the layered or banded sulfides increase in abundance from south to north (Fig. 2). Massive sulfide breccias and late breccias composed of tan sphalerite are prevalent in Qanaiyaq and the Main deposit but are rarely observed in Aqqaluk or Paalaaq. In contrast, layered or banded sulfides in barite or shale appear to be absent in Qanaiyaq and are rarely and erratically distributed in the Main deposit, but they are abundant in parts of the Aqqaluk and Paalaaq deposits.

Among the four Red Dog deposits, there is an apparent geochemical zoning (Fig. 2). Qanaiyaq and the Main deposit have higher average Pb and Zn grades than Aqqaluk and Paalaaq. Qanaiyaq averages 17.8 percent Zn and 5.5 percent Pb, the Main deposit has average grades of 19.5 percent Zn and 5.3 percent Pb, and Aqqaluk has 13.7 percent Zn and 3.6 percent Pb. On the basis of available drilling, Paalaaq is slightly lower grade than Aqqaluk. Copper concentrations reach >0.1 percent in Qanaiyaq but are much lower in the other deposits, whereas iron increases from south to north. Qanaiyaq averages 7.5 percent Fe, the Main deposit contains 7.9 percent Fe, Aqqaluk has close to 8.5 percent Fe, and Paalaaq contains more than 10 percent Fe (T. Krolak, pers. commun., 2002).

Vertical geochemical zoning in the deposits is evident from variations in Zn/Fe and Zn/Pb ratios for the Main deposit (Sims, 1996) and Aqqaluk (T. Krolak, writ. commun., 2003) (Fig. 2). The Zn/Fe ratios increase from sulfide-bearing barite to “regular” massive sulfide ore (excluding irregularly distributed Fe-rich portions) and decrease in basal vein ore. Average Zn/Fe ratios for sulfide-bearing barite for both the Main and Aqqaluk deposits combined are 2.6, massive sulfide ore averages 4.0, and vein ore averages 1.5. The Zn/Pb ratio increases from top to bottom, with an average Zn/Pb ratio of 3 in the sulfide-bearing barite, 4.4 in the massive sulfide ore, and 4.5 in the vein ore. The vertical geochemical variations may reflect changes in the overall abundances of ore minerals, or alternatively, they could reflect the chemical composition of the sulfides. For example, there is a greater abundance of iron sulfide in vein ore compared with regular massive sulfide ore, and sphalerite in vein ore is Fe rich compared with that in other ore types (discussed below).

Mineralogy, Textural Variations, and Paragenesis

A paragenetic sequence for the Red Dog deposits (Fig. 4) was developed from drill core, hand specimens, and thin section samples (Figs. 5 and 6). The stages are defined primarily by sphalerite type and summarized as follows: (1) early deposition of barite, early brown sphalerite, pyrite, and minor galena on or immediately beneath the sea floor; (2) hydrothermal recrystallization of previously formed barite and deposition of yellow-brown sphalerite; (3) deposition of barite, red-brown sphalerite and other sulfides in open space veins and coeval replacement of barite; and (4) late-stage, postore formation of late tan sphalerite breccias (Fig. 4) and deposition of minor barite, pyrite, witherite, and calcite in late veins and open vugs.

Sulfides deposited during the four stages are texturally distinct, and sphalerite exhibits marked compositional differences between stages. Stage 1 and 4 sulfides are volumetrically minor, whereas stages 2 and 3 form the bulk of the ore (Fig. 4). Silica is a major constituent of the ore deposits and adjacent wall rocks. The timing of silicification remains controversial. Slack et al. (2004b) suggest that some silica in and around the orebodies was introduced with the metal-bearing ore fluid (just prior to or with stage 2 fluids), whereas Leach et al. (2004) suggest that the majority of the silica was deposited after main stage mineralization. The focus of this paper is on the barite and sulfide minerals.

Stage 1

Fine- to medium-grained barite (\pm sulfides) is typically observed at the stratigraphic top of the deposits in black mudstone or shale (Fig. 3). The distribution of this assemblage may have been more extensive, but main-stage sulfide mineralization (described below) and postore silicification (Leach et al., 2004) have obscured the original distribution.

Sulfide minerals that coprecipitated with early barite include dark- to light-brown sphalerite, minor pyrite, and traces of galena (Fig. 4). On a deposit scale, brown sphalerite is volumetrically minor. However, it is the dominant sulfide in the stage 1 assemblage. In all thin sections containing brown sphalerite, it is present in proportions equal to barite, and it is at least twice as abundant as pyrite or galena.

Stage 1 barite is white or light gray and is present as irregularly distributed crystals (up to 0.5 cm long but generally smaller) or thin laminae in black shale or mudstone (Figs. 5A, 6A), as equigranular aggregates (10–50 μ m) intergrown with colloform or dendritic brown sphalerite (Figs. 5B, 6B-E), or as irregular, discontinuous wispy layers alternating with sphalerite (Figs. 5C, 6F). Ores containing the latter two types are generally free of sediment.

In samples of mudstone, compaction features and disruption of laminae by barite crystals (Fig. 6A) indicate that barite formed in unconsolidated sediment. Early barite of stage 1 is commonly intergrown with early brown sphalerite. Colloform

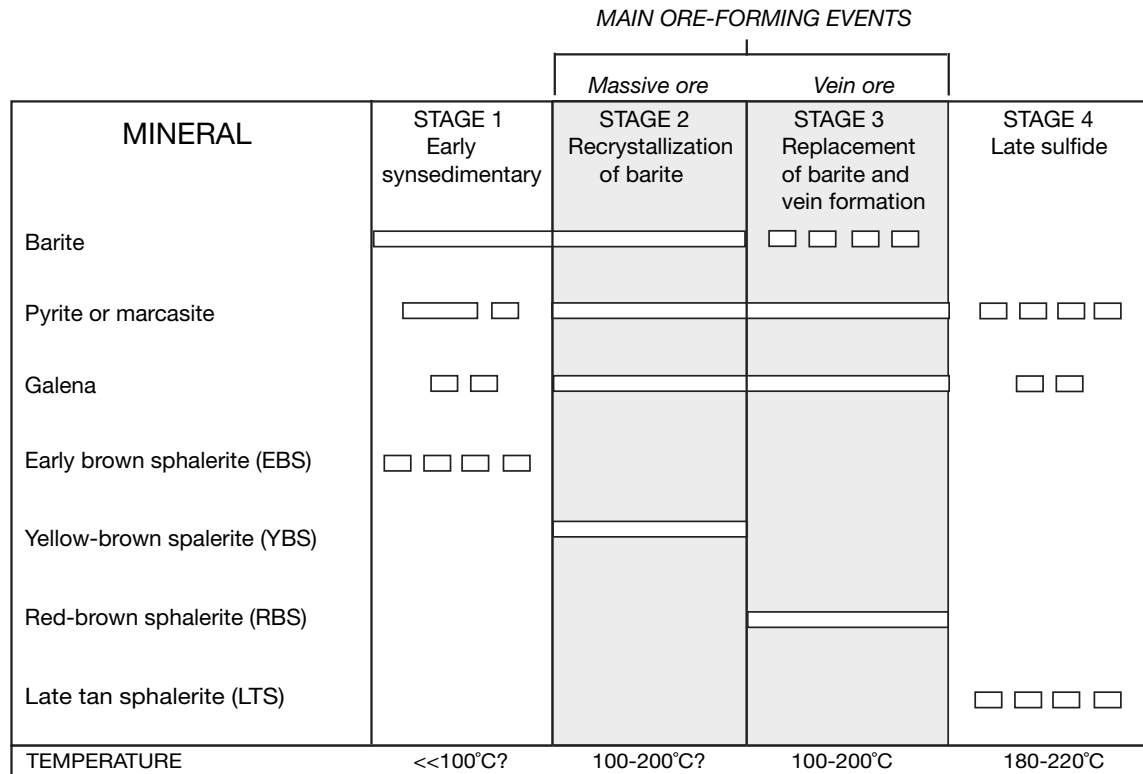


FIG. 4. Simplified paragenetic sequence of sulfides and barite from the Red Dog deposits. Stages are defined primarily by sphalerite type. Temperatures for stage 3 sphalerite were determined by fluid inclusion microthermometry (Leach et al., 2004). Temperatures for other stages are estimates (see text). Solid bars represent the distribution of major minerals within a given stage; four broken bars represent minor occurrences; two broken bars represent trace occurrences. Stages 1 and 4 are volumetrically minor in the deposits overall, whereas stages 2 and 3 form the bulk of the ore. Other minerals present in the deposits, such as quartz, chalcopyrite, calcite, and witherite are not shown on the diagram but are discussed in the text.

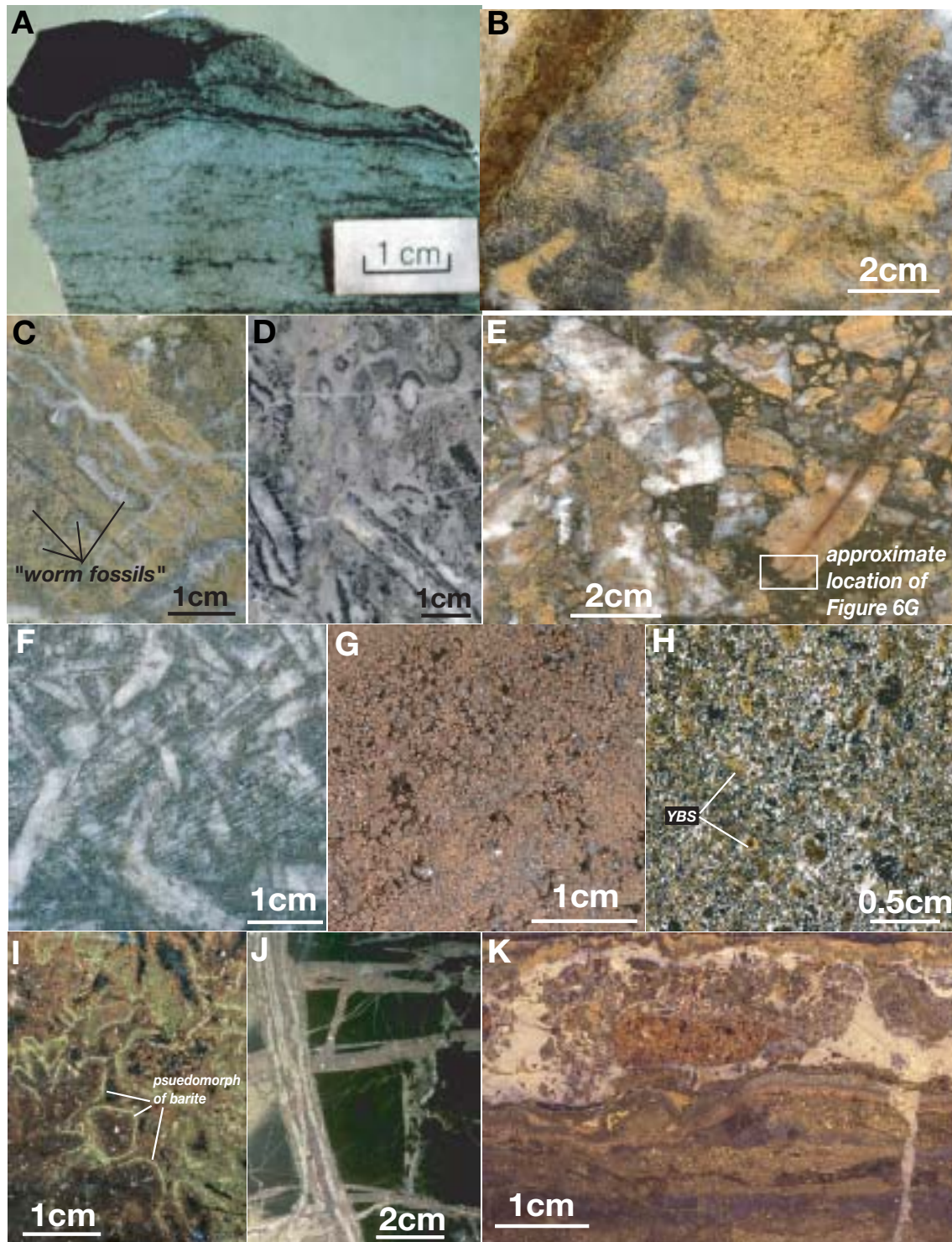
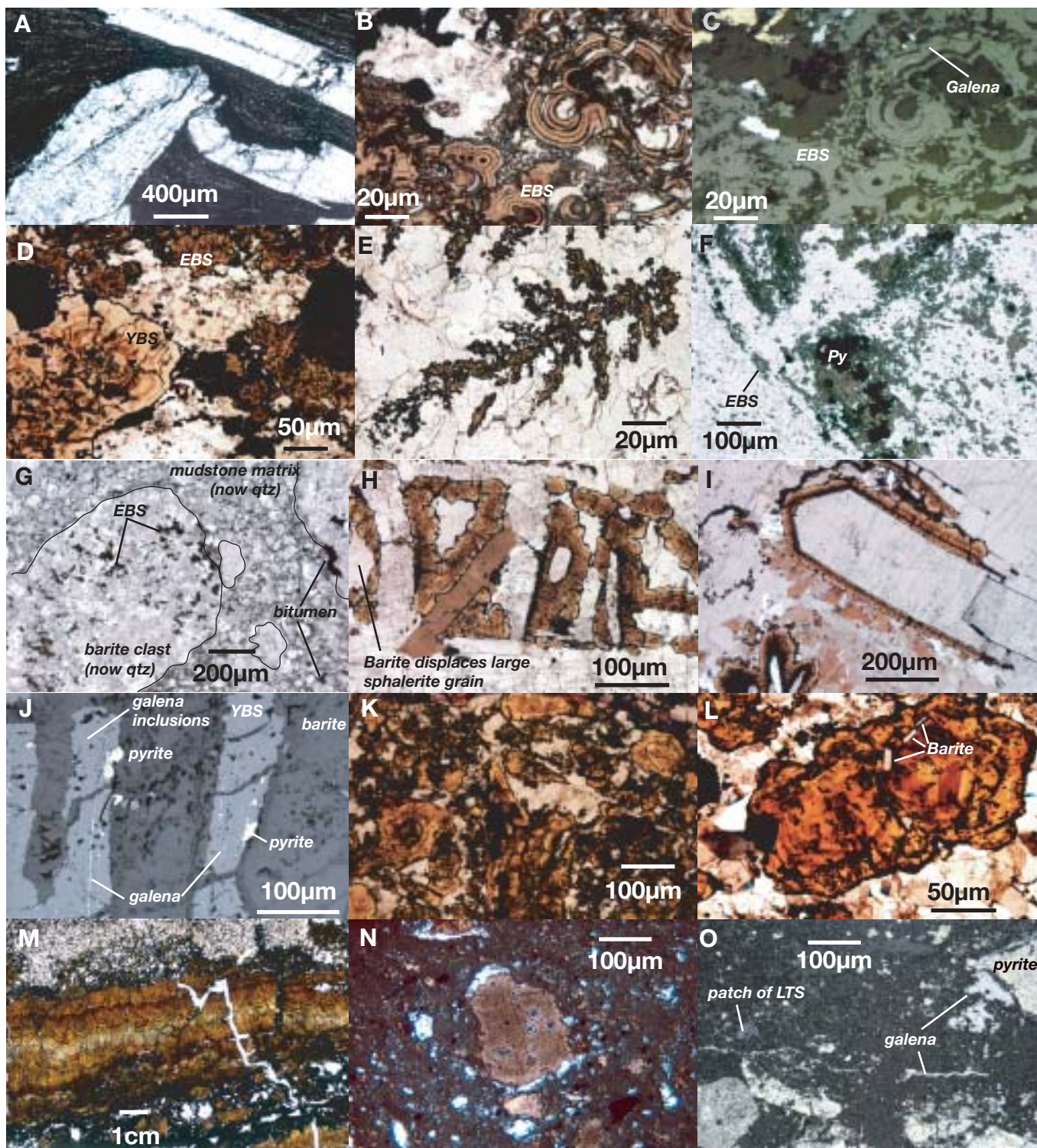


FIG. 5. Hand samples showing textural variations of different ore types from the Red Dog deposits. A. Sulfide-poor barite in Ikalukrok unit shale and mudstone. B. Fine-grained barite and dendritic early brown sphalerite. C. Barite and early brown sphalerite with layered appearance. Note the presence of the elongated "worm fossil" filled with barite. D. Silicified barite and early brown sphalerite showing abundant worm tubes. E. Hand sample showing clasts of early brown sphalerite and barite in a black mudstone matrix. F. Sulfide-bearing barite from the top of the Aqqaluk deposit showing extremely coarse-grained barite (up to 3 cm) with interstitial fine- to medium-grained sulfides (dark). G. Typical coarse-grained massive sulfide ore showing sulfides disseminated in dark matrix that appears to be mudstone. H. Thin section photograph of same sample as that in H showing grains of yellow-brown sphalerite in quartz matrix. I. Sample showing complete replacement of former large euhedral barite crystals by pyrite (forming rims), followed by red-brown sphalerite that fill the center of former barite crystals. J. Planar veins cutting silicified mudstone. Note multiple sets. K. Late tan breccia cutting vein ore. Note clasts of red-brown sphalerite and vein ore. YBS = yellow-brown sphalerite.



brown sphalerite forms well-defined, micrometer-scale bands that alternate with bands of barite (Fig. 6B-D). Locally, brown sphalerite appears to be partially replaced by barite because it is present as rounded aggregates floating in a barite matrix (Fig. 6B). Minor galena is present as thin, discontinuous, micrometer-scale bands with sphalerite (Fig. 6C). Subhedral pyrite with highly irregular grain boundaries is intimately intergrown with barite and sphalerite (Fig. 6D). Some of these pyrite grains enclose brown sphalerite or barite.

A more common form of early brown sphalerite is dendritic intergrowths with barite (Fig. 6E). As with the colloform variety, the dendritic sphalerite is typically observed in unsilicified barite. Barite and sphalerite are equigranular and fine-grained, averaging about 10 to 50 μm , but locally grains coalesce to form patches that are 100 μm in size. Dendritic textures are interpreted as having formed by rapid coprecipitation from supersaturated solutions that limits growth of large crystals (cf. Naslund et al., 1984; Frisia et al., 2000).

In the northwest portion of Aqqaluk and in Paalaaq, barite and early brown sphalerite display a crude layering in hand samples (Fig. 5C). Examination of thin sections reveals minimal layering, but there is a discontinuous alignment of early brown sphalerite (Fig. 6F). In some of these samples, structures referred to as "worm fossils" are a notable feature (Fig. 5C-D). These structures are cylindrical with dimensions of a few millimeters wide and up to 10 cm long. Moore et al. (1986) interpreted them to be fossil remnants of a vent-specific fauna analogous to modern sea-floor tube worms (Moore et al., 1986). More recent work suggests that the structures are tube walls, now composed of quartz, but originally secreted by annelid-like organisms that lived in a variety of settings within the Kuna basin (Anderson et al., in prep.). Worm tubes are most commonly observed in silica rock (silicified sulfide-bearing barite; Fig. 5D), probably because silicification sharpens the contrast between the wall and center of the structure.

The textural evidence from Red Dog is permissive for formation of early barite and sulfides on or immediately below the sea floor. Compaction of surrounding mudstone and

disruption of mudstone laminae by some barite crystals (Fig. 6A) are evidence that barite formed during sedimentation and before lithification of the sediments. At least some of the sediment-free massive and irregular accumulations of fine-grained barite and sulfides may have formed in the water column above the sediment-seawater interface, although textural evidence to evaluate this is lacking, owing to the widespread silicification of barite at Red Dog. One drill hole through the Aqqaluk deposit intersected a breccia that consists of what appear to be subangular to angular clasts of early brown sphalerite and barite in a black mudstone matrix (Fig. 5E). However, in thin section the sample is so thoroughly silicified that any original primary textures have been obliterated (Fig. 6G). One possibility for the origin of the brecciated texture is that it formed by slumping of barite and sphalerite into a baritic mud on the sea floor. Alternatively, its origin may be similar to breccias in modern sediment-hosted sea-floor sulfide deposits (e.g., Middle Valley; Ames et al., 1993) that form by collapse of a mound through dissolution or replacement of anhydrite. Replacement of carbonate is another possibility.

Stage 2

Precipitation of early brown sphalerite was followed by yellow-brown sphalerite and the beginning of main-stage ore formation. Evidence for the relative timing includes crosscutting relationships and overgrowths of yellow-brown sphalerite on early brown sphalerite (Fig. 6D). Yellow brown sphalerite is volumetrically the most significant sulfide in the Red Dog deposits and is the dominant sulfide mineral in sulfide-bearing barite, silica rock (silicified sulfide-bearing barite), and massive sulfide ore. Together these ore types make up about 78 percent of the total tonnage being mined.

Yellow-brown sphalerite and other sulfide minerals are present interstitial to sulfide-bearing barite (Figs. 5F, 6H-J). In contrast to the early barite, the barite associated with yellow-brown sphalerite is white and extremely coarse grained with individual crystals forming euhedral prisms up to 3 cm long (Fig. 5F). Sulfide grain sizes range from 50 to 200 μm . Yellow-brown sphalerite crystals are typically elongate and have

FIG. 6. Photomicrographs showing textural variations of barite and sulfide minerals. A. Barite crystals (some doubly terminated) in Ikalukrok unit shale and mudstone showing compaction of surrounding mudstone laminae; note that barite crystals also disrupt mudstone laminae. B. Early brown sphalerite as micrometer-scale bands intergrown with barite (plane light). C. Same as B, but in reflected light; note tiny galena band (high reflectance) in sphalerite. D. Early brown sphalerite and stage 2 yellow-brown sphalerite with barite (plane light). E. Early brown sphalerite and barite showing dendritic intergrowths (plane polarized light); barite is equigranular and fine-grained (individual barite grains average about 10 μm). F. Early brown sphalerite and fine-grained barite in sample showing "layered" appearance (Fig. 5C). Although early brown sphalerite is crudely aligned as wispy discontinuous layers, it is mostly disseminated in fine-grained barite. G. Breccia (shown in Fig. 5E) showing thorough silicification; late silica has replaced barite both in clasts and the matrix of the muds, obliterating any primary textural features on a microscopic scale. H. Yellow-brown sphalerite and barite showing typical texture in coarse-grained sulfide-bearing barite. Yellow-brown sphalerite formed mostly interstitial to barite, and therefore has triangular shape. Note left-hand portion of slide where barite crystals appear to disrupt and fragment previously formed yellow-brown sphalerite crystal (plane polarized light). I. Yellow-brown sphalerite and pyrite (opaque) grew on euhedral barite crystals in open space, followed by infilling of relatively finer-grained barite (plane polarized light). J. Barite with pyrite and yellow-brown sphalerite; galena forms infilling in center of sphalerite grains. Note tiny inclusions of galena in yellow-brown sphalerite (reflected light) and irregular contact between yellow-brown sphalerite and barite. K. Yellow-brown sphalerite rosettes and fragments in quartz in massive sulfide. Opaque mineral is galena. L. Grain of yellow-brown sphalerite with small euhedral barite crystals aligned along growth zone. M. Red-brown sphalerite in vein cutting massive sulfide. Note color banding in red-brown sphalerite. N. Late tan sphalerite and very fine grained silica. Note euhedral crystals of quartz in late tan sphalerite (plane polarized light). O. Breccia with late tan sphalerite and fine-grained silica in the matrix and clasts of fractured and broken pyrite, and smeared grains of galena around pyrite or in fractures. EBS = early brown sphalerite, LTS = late tan sphalerite, YBS = yellow-brown sphalerite.

triangular shapes as a result of having formed interstitial to, or as epitaxial growths on, large barite crystals (Fig. 6H-I). Abundant textural evidence suggests that, like early brown sphalerite, precipitation of yellow-brown sphalerite overlapped and alternated with deposition of barite. The growth of large barite blades disrupted, relocated, and fragmented sphalerite crystals that had previously formed or were forming during barite growth (Fig. 6H). In some samples, yellow-brown sphalerite and other sulfides grew on previously formed euhedral barite crystals in what appears to have been open space, followed by infilling of relatively finer-grained barite (Fig. 6I). Locally, irregular grain boundaries between barite and yellow-brown sphalerite (Fig. 6I-J) suggest that yellow-brown sphalerite partially replaced barite.

Intergrowths and inclusions of galena in yellow-brown sphalerite are common features of stage 2 (Fig. 6J). Pyrite is anhedral to euhedral and free of sphalerite or barite inclusions. Where pyrite is present, the typical sequence of deposition was pyrite followed by yellow-brown sphalerite and then galena.

Yellow-brown sphalerite, galena, and pyrite are present as disseminated 50- to 200- μm grains in massive sulfide ore below sulfide-bearing barite (Figs. 5G-H, 6K-L). As in sulfide-bearing barite, yellow-brown sphalerite is commonly intergrown with galena. In hand samples, the sulfide grains appear disseminated in black mudstone (Fig. 5G), but thin section examination reveals a dense silica matrix (Fig. 6K-L). Petrographic and fluid inclusion studies show that the silica in these rocks replaced preexisting barite (Leach et al., 2004). Thus, prior to silica introduction, most massive sulfide originally consisted of barite and sulfide minerals. The presence of small euhedral barite crystals aligned along sphalerite growth zones is direct evidence of sulfide and barite coprecipitation during formation of massive sulfide (Fig. 6L).

Massive sulfide ore is locally fragmental or clastic in appearance (Fig. 5H) and has been interpreted by previous workers as having formed in situ by "invasions of growth zoned crustiform sphalerite that disrupted the rock" (Moore et al., 1986), by sedimentary processes (Moore et al., 1986; Edgerton, 1997), or through brecciation (Edgerton, 1997). Some yellow-brown sphalerite in massive sulfide ore appears to be angular and broken fragments of originally larger grains (Fig. 6K), and many fragments show a strong resemblance to yellow-brown sphalerite grains in sulfide-bearing barite (Fig. 6H). For example, the elongate fragment in the center of Figure 6K may have been sphalerite and galena that originally grew on or interstitial to barite. Thus, some of the fragmentation probably occurred during stage 2 barite crystal growth where preexisting grains of yellow-brown sphalerite were disrupted. However, because fragmental textures are most prevalent in massive sulfide ore (i.e., silicified barite and sulfides), it is probable that late silicification also contributed to the fragmental textures (Leach et al., 2004).

Stage 3

Coarse-grained, red-brown sphalerite marks stage 3 or the late main ore stage (Fig. 4). Red-brown sphalerite replaces barite and also is present in vein ore, which constitutes about 21 percent of the total tonnage mined. The mineralogy of the veins consists of barite, red-brown sphalerite,

pyrite, marcasite, galena, calcite, growth zoned quartz, and chalcedonic silica.

Red-brown sphalerite was deposited after coarse barite (stage 2), and red-brown sphalerite pseudomorphs after barite are up to 2 cm long (Fig. 5I). Red-brown sphalerite also is present in veins and spatially associated breccias that cut silicified shale or mudstone (Fig. 5J), silica rock (preexisting sulfide-bearing barite), and massive sulfide ore (Fig. 6M). Multiple episodes of polymetallic veining with red-brown sphalerite are evident (Fig. 5J). The veins of sphalerite exhibit color variation (Fig. 6M) that corresponds with compositional zonation (discussed below). Colors range from nearly colorless to yellow to orange to dark red. Red-brown sphalerite typically contains abundant pyrite inclusions with rare minute inclusions of pyrrhotite, chalcocopyrite and tetrahedrite.

The light-dark zonation of red-brown sphalerite sometimes parallels the vein walls, but banding of individual sphalerite grains and symmetry of color banding in the veins is not uniform. Dark-colored sphalerite predating light-colored sphalerite and light-colored sphalerite predating dark sphalerite are equally common. Optically continuous sphalerite crystals transgress the color zones, suggesting some recrystallization occurred after deposition. Subordinate coarse-grained pyrite, marcasite, and galena also form bands parallel to vein walls (Fig. 5J), but the order in which these minerals are found from wall to center within the veins is not consistent.

The dominant gangue mineral associated with stage 3 veins is quartz; barite and calcite are volumetrically minor. Quartz and barite form infillings in the center of the veins but also are present along vein margins (Moore et al., 1986). Most of the quartz is white and distinctly zoned (Leach et al., 2004). Strikingly different, minor gray-blue chalcedonic quartz is present in the centers of some veins (Slack et al., 2004b). Petrographic observation using cathodoluminescence and the scanning electron microscope indicate that much of the growth-zoned quartz in the veins replaced preexisting barite, whereas the chalcedonic quartz may have been deposited contemporaneously with sulfides (Slack et al., 2004b).

Stage 4

Late tan sphalerite defines stage 4 (Fig. 4), which is represented exclusively in 1- to 10-cm wide breccias (Fig. 5K) that cut all rock and ore types. The breccias are present predominantly in the Qanaiyaq and Main deposits and less commonly in the Aqqaluk deposit; they have not been described at other deposits in the district. Although they are economically insignificant and not mappable as separate units, they do mark the last mineralizing event in the Red Dog deposits. Late tan sphalerite is present with silica in the matrix of the breccias. Although patches (up to 100 μm) of nearly pure late tan sphalerite are present locally, the matrix typically consists of finely intergrown late tan sphalerite and silica (Fig. 6N-O). In some thin sections, subhedral to euhedral quartz crystals enclosed in patches of sphalerite (Fig. 6N) and trains of sphalerite grains along growth zones within individual quartz crystals suggest coeval deposition of sphalerite and silica.

Clasts in the breccias are composed of earlier-formed vein minerals and silicified shale (Fig. 5K). Pyrite is present as fractured and broken grains, whereas galena is plastically deformed into irregular fractures (Fig. 6O). Galena in these late

breccias also displays curved cleavages. The overall fine grain size of the sulfides (especially sphalerite) and deformation styles of pyrite and galena suggest that the breccias formed by cataclastic tectonic processes like those described by Marshall et al. (2000), most likely at the onset of Brookian orogenesis or metamorphism at about 190 to 170 Ma (Moore et al., 1994; Rombach and Layer, 2004). If the breccias are Brookian, they formed more than 100 m.y. after the main stage of Zn-Pb mineralization.

Minor barite, calcite, and witherite veins cut earlier barite at Red Dog, and euhedral pyrite and barite are present with growth-zoned quartz in late vugs and veinlets throughout the deposit. Witherite is characterized by consistently low $\delta^{18}\text{O}$ values that were interpreted by Leventhal et al. (2002) to indicate precipitation from meteoric water sometime after the Zn-Pb mineralization. White mica associated with quartz and pyrite in a vug from the Main deposit yields a $^{40}\text{Ar}/^{39}\text{Ar}$ age of 126.1 ± 0.7 Ma, suggesting that these minerals formed during the Brookian orogeny (Rombach and Layer, 2004).

Trace Elements in Sphalerite and Pyrite

Sphalerite

The analyses of sphalerite by LA-ICP-MS are presented in Table 1 and Figures 7 and 8. A total of 204 analyses (32 of early brown sphalerite, 88 of yellow-brown sphalerite, 40 of red-brown sphalerite, and 44 of late tan sphalerite) were obtained from 27 samples. Stage 2 and 3 sphalerite (yellow-brown and red-brown sphalerite) were analyzed from all four deposits, but stage 1 sphalerite (early brown sphalerite) was not observed in Qanaiaq or Paalaaq, and stage 4 sphalerite (late tan sphalerite) was not found in Paalaaq.

Distinct chemical differences exist between the sphalerite types, particularly with regard to Fe, Co, Mn, Tl, and Ge. Bivariate plots (Fig. 7) and comparison of mean concentrations (Fig. 8) show a general trend of increasing Fe and Co and decreasing Mn, Tl, and Ge from early brown to later ore-stage yellow-brown and red-brown sphalerite, with the latter two types displaying much more compositional variation. Fe and Mn concentrations in early brown sphalerite range from 0.7 to 1.9 wt percent and 5 to 37 ppm, respectively, whereas Fe concentrations in yellow-brown and red-brown sphalerite are two to four times as high and Mn contents are less than 27 ppm. Significantly higher Co (310 ppm in yellow-brown sphalerite and 382 ppm in red-brown sphalerite compared with <63 ppm in early brown sphalerite) and lower Tl also characterize ore-stage sphalerite (Table 1). The range in compositions of red-brown sphalerite correlates with color banding; nearly colorless bands contain 0.7 to 3 wt percent Fe, orange-yellow bands contain 3 to 6 wt percent Fe, and dark red zones contain >6 wt percent Fe. Other elements such as Co show a similar though less consistent correlation with color. The late tan sphalerite has distinctly lower Fe (< 0.9 wt %) and Co (<11 ppm), and higher Tl (up to 355 ppm) and Mn (up to 177 ppm) compared with all earlier sphalerite. Concentrations of Ge are variable, but the average concentration in late tan sphalerite is significantly greater (249 ppm) than that of all earlier sphalerite (<200 ppm).

Elements such as Ag, Cu, Pb, and Sb display wide ranges of concentration for in all sphalerite types, particularly yellow-

brown and red-brown sphalerite (Fig. 7). Similar patterns are observed for As and Hg (not plotted). There is an overall positive correlation between Ag and Pb and good correlations between Ag and Sb and Cu and Sb, although the concentrations of these elements in yellow-brown and red-brown sphalerite vary greatly. For example, Ag concentrations in red-brown sphalerite range from 4 to 1,720 ppm (Table 1). Concentrations of Cu and Sb are similarly variable, and Cu ranges from 16 to 2,820 ppm in yellow-brown sphalerite, and Sb from 18 to 3,560 ppm in red-brown sphalerite. Erratic high values of Pb characterize all four sphalerite types (Table 1 and Fig. 7).

Good correlations between Ag and Sb, Cu and Sb, and to a lesser extent Ag and Pb, and the wide ranges of these elements in nearly all sphalerite types suggest that these elements probably reside in galena, chalcopyrite, and/or tetrahedrite inclusions. The fact that the Sb/Cu molar ratios of yellow-brown and red-brown sphalerite are consistent and close to the 3:1 molar ratio expected for tetrahedrite further suggests that these elements are present in inclusions of tetrahedrite (Fig. 7). However, the data do not preclude the possibility that some of these elements also reside as lattice substitutions.

Elements most likely residing in the sphalerite lattice are Fe, Cd, Mn, Tl, Co, and Ge as suggested by their consistent distributions within and among the different types of sphalerite (Fig. 7). Sphalerite commonly contains MnS, CdS, and CoS in solid solution (Vaughan and Craig, 1997), and experimental studies by Jiuling (1993) have shown that up to 1,500 ppm Tl can be incorporated in natural sphalerites. Some of the high Tl and Co in the sphalerite may reflect inclusions of pyrite, which typically contains high concentrations of these elements (discussed below). However, the sphalerite that contains the most abundant visible pyrite (red-brown sphalerite) has the lowest Tl contents and, therefore, pyrite inclusions could not have been a major contributor to the sphalerite chemistry.

Pyrite

Table 2 and Figure 9 summarize the trace element data for pyrite. A total of 62 analyses are reported. Unlike sphalerite, most trace elements in pyrite from stages 1 through 3 lack systematic variations. The highly variable Ag, As, Sb, and Tl contents in stage 1 pyrite significantly overlap with those of stages 2 and 3. Concentration ranges in stages 1 through 3 are 6 to 900 ppm Ag, 16 to 10,750 ppm As, 2 to 5,580 ppm Co, 3 to 2,160 ppm Cu, 7 to 6,720 ppm Sb, and 2 to 12,220 ppm Tl (Table 2).

Geochemical variations for many elements in pyrite associated with late tan sphalerite in stage 4 breccias are distinctly different (Fig. 9 and Table 2). In particular, this stage of pyrite has significantly lower contents of Ag (<100 ppm), Co (<80 ppm), Tl (<41 ppm), Cu (<136 ppm) and Ni (<14 ppm). Pyrite in shale of the Kuna Formation away from known mineralization has similar low values of most trace elements, particularly Ag and Tl (Slack et al., 2004b).

If the stage 4 breccias formed by fluids related to the Brookian orogeny, the trace element signatures of stage 4 pyrite may reflect the release of trace elements in local pre-existing sulfide minerals during diagenesis and metamorphism. Studies of trace element contents in pyrite from vol-

TABLE 1. Basic Statistics for Minor and Trace Element Contents in Sphalerite from the Red Dog Deposits

	Min	Mean	Median	25th	75th	Max	% above MDL
Stage 1: Early brown sphalerite, $n = 32$, deposits M, A							
Fe wt %	0.7	1	1	0.8	1.3	1.9	100
Cd	0.1	0.4	0.4	0.4	0.5	0.6	97
Ag	56	381	226	144	279	1,500	100
As	4	175	42	18	192	2,100	100
Co	9	39	43	27	52	63	94
Cu	33	591	360	254	681	1,990	100
Ge	54	192	149	108	244	423	100
Hg	13	283	80	64	187	1,810	91
Mn	5	20	20	14	26	37	91
Pb	31	3,651	2,390	965	5,990	9,830	97
Sb	32	595	307	174	546	2,520	100
Tl	11	43	31	21	49	126	100
Cu/Ag	.6	2	1.4	1.2	2	5	100
Stage 2: Yellow-brown sphalerite, $n = 88$, deposits Q, M, A, P							
Fe wt %	0.6	1.9	2	1.5	2.4	4.2	100
Cd	0.2	0.5	0.5	0.4	0.6	0.9	100
Ag ppm	5	172	129	79	199	758	100
As	0.05	48	27	7	68	294	95
Co	11	122	102	74	176	310	100
Cu	16	745	574	293	1,082	2,820	100
Ge	1.5	104	103	65	143	261	100
Hg	18	181	77	44	212	1,460	97
Mn	0.7	8	7	5	9	27	94
Pb	4	822	332	103	1,428	5,730	92
Sb	0.5	480	343	151	673	2,440	100
Tl	0.07	6	3	1.6	8	37	91
Cu/Ag	1	5	4	3	6	27	100
Stage 3: Red-brown sphalerite, $n = 40$, deposits Q, M, A, P							
Fe wt %	0.7	3	3	1.8	4	7.3	100
Cd	0.2	0.4	0.4	0.3	0.5	1	100
Ag ppm	4	219	94	45	238	1,720	100
As	0.9	168	52	9	222	916	93
Co	14	149	149	82	207	382	98
Cu	88	438	335	164	533	1,610	100
Ge	14	116	82	47	160	425	100
Hg	18	727	108	61	1,192	3,650	100
Mn	1.3	11	11	5	16	23	93
Pb	0.8	366	212	79	557	2,030	98
Sb	18	464	204	57	629	3,560	100
Tl	0.3	5	5	1.5	8.2	15	95
Cu/Ag	0.4	6	3	2	6	103	100
Stage 4: Late tan sphalerite, $n = 44$, deposits Q, M, A							
Fe wt %	0.1	0.3	0.3	0.2	0.4	0.9	100
Cd	0.3	0.6	0.8	0.6	0.8	0.9	98
Ag ppm	144	373	359	243	497	640	100
As	2	39	15	9	41	264	98
Co	0.6	3	2	0.8	4	11	89
Cu	29	319	332	238	436	525	100
Ge	100	249	247	191	288	426	100
Hg	10	177	46	30	106	1,570	95
Mn	28	77	67	57	88	177	100
Pb	61	1,585	919	325	2,072	8,750	100
Sb	266	450	430	335	539	774	100
Tl	15	141	140	62	190	355	100
Cu/Ag	0.1	0.9	0.9	0.5	1	3	100

A = Aqqualuk, M = Main, Max = maximum value, MDL = minimum detection limits, Min = minimum value, P = Paalaaq, Q = Qanaiyaq, 25th = 25th percentile, 75th = 75th percentile

Values for minimum MDL vary, but maximum MDL for this data set are as follows: Fe = 0.01, Cd = 0.05, Ag = 0.05, As = 0.05, Co = 0.5, Cu = 0.5, Ge = 0.5, Hg = 0.1, Mn = 0.5, Pb = 0.5, Sb = 0.5, Tl = 0.05

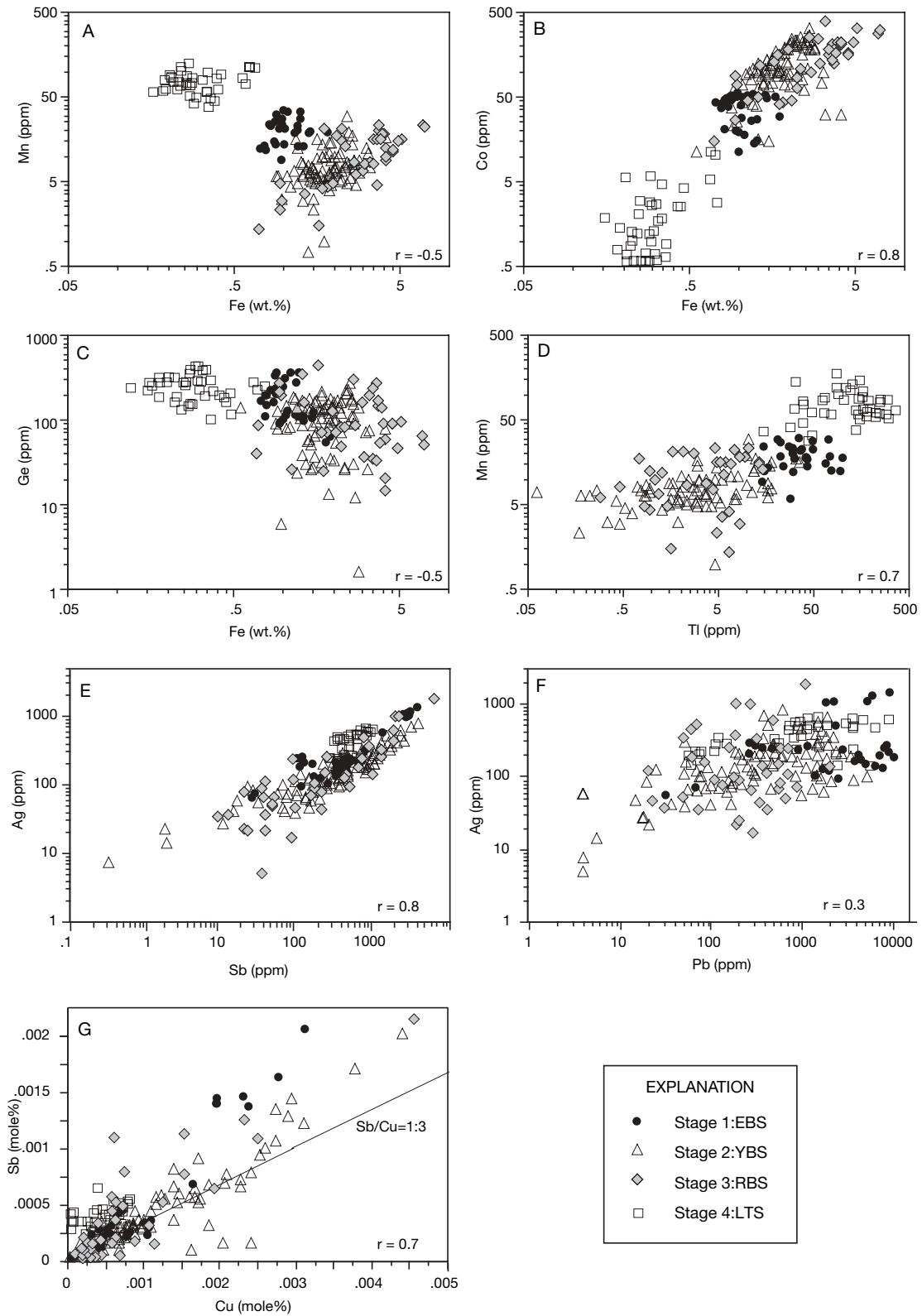


FIG. 7. Bivariate plots of trace element concentrations determined by LA-ICP-MS in the four stages of sphalerite from the Red Dog deposits. A. Mn vs. Fe. B. Co vs. Fe. C. Ge vs. Fe. D. Mn vs. Tl. E. Ag vs. Sb. F. Ag vs. Pb. G. Sb vs. Cu in mol percent; line showing Sb/Cu = 1:3 is typical stoichiometric ratio of Sb and Cu in tetrahedrite. Fe values in wt percent, other elements in parts per million. Correlation coefficients calculated from analyses in which both elements exceeded the detection limits are shown for each diagram. See Table 1 for statistics of each sphalerite stage. EBS = early brown sphalerite, LTS = late tan sphalerite, RBS = red-brown sphalerite, YBS = yellow-brown sphalerite.

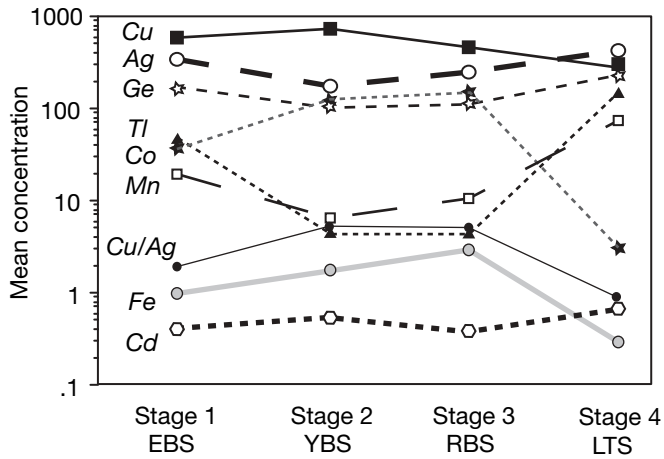


FIG. 8. Comparison of mean concentrations of Ag, Cd, Co, Cu, Ge, Fe, Mn, Tl, and Cu/Ag determined by LA-ICP-MS in stages 1 through 4 sphalerite from the Red Dog deposits. All elements in parts per million except Fe and Cd, which are in percent. See Table 1 for data statistics.

canogenic massive sulfide deposits suggest that elements like Cu, Ag, As, and Tl that are present as inclusions are mobilized during hydrothermal and metamorphic recrystallization (Huston et al., 1995). Thus, Cu, Ag, As, and Tl in early pyrite at Red Dog may have been leached during circulation of seawater or by burial and metamorphic dewatering related to the Brookian orogeny.

Sulfur Isotopes

The results of sulfur isotope analyses are listed in the Appendix and shown on Figures 10 and 11. Sulfides have a wide range of $\delta^{34}\text{S}$ values from -45.8 to 12.3 per mil, with a majority at about -2.5 to 7.5 per mil (Fig. 10). Isotopic data produced by analyses of bulk mineral separates cluster around zero per mil (Schmidt and Zierenberg, 1988; Zierenberg and Schmidt, 1988), consistent with the major population determined by the ion microprobe.

Data for specific minerals include 77 analyses of sphalerite, 31 analyses of galena, and 25 analyses of pyrite (Fig. 11). A striking feature of the sphalerite data is the close correlation

between texture or paragenetic stage and $\delta^{34}\text{S}$ values. Early formed, fine-grained, early brown sphalerite has primarily negative values, whereas coarser disseminated or interstitial sulfides that form the main ore stages 2 and 3 (yellow-brown and red-brown sphalerite) have significantly higher values (means of yellow-brown and red-brown sphalerite are 3.3 and 3.4‰, respectively). Late-stage late tan sphalerite samples all have low $\delta^{34}\text{S}$ values (Fig. 11).

Although nearly all $\delta^{34}\text{S}$ values of early brown sphalerite are negative, the $\delta^{34}\text{S}$ composition varies with texture. The mean value is -33.3 per mil ($n = 13$) for colloform early brown sphalerite, -5.7 per mil ($n = 2$) for dendritic sphalerite and -0.4 per mil ($n = 3$) for layered sphalerite. These variations may record differences in the extent of bacteriogenic fractionation (discussed below). Alternatively, the higher $\delta^{34}\text{S}$ values of dendritic and layered forms compared with colloform early brown sphalerite may reflect contamination from adjacent barite, which is isotopically heavy (Fig. 10). All forms of early brown sphalerite are intergrown with barite, but colloform varieties commonly are present as aggregates up to 200 μm in diameter that are free of microscopically visible barite or other sulfide minerals.

Data for pyrite follow a similar pattern. Pyrite associated with colloform early brown sphalerite has $\delta^{34}\text{S}$ values as low as -45.8 per mil (Appendix and Fig. 11), whereas pyrite in massive sulfide (stage 2) and vein ore (stage 3) have higher values from -27.3 to 9.9 per mil. Similar to late tan sphalerite, pyrite in late stage 4 breccias has low negative $\delta^{34}\text{S}$ values.

Sulfur in stage 2 and 3 ore-related galena is isotopically lighter than that of associated sphalerite and shows a small range in composition. Stage 2 galena has a mean $\delta^{34}\text{S}$ value of 0.8 per mil ($n = 11$), whereas galena from vein ore (stage 3) has a mean value of -2.5 per mil ($n = 6$). Stage 1 galena analyzed by ion microprobe does not have the negative values of early brown sphalerite or stage 1 pyrite (Fig. 11). However, a galena separate from one stage 1 sample containing dendritic early brown sphalerite and barite, analyzed by conventional techniques, has a value of -14.3 per mil (C.A. Johnson, unpub. data). The most likely explanation for the high $\delta^{34}\text{S}$ values of stage 1 galena is that the ion microprobe analyses included traces of barite.

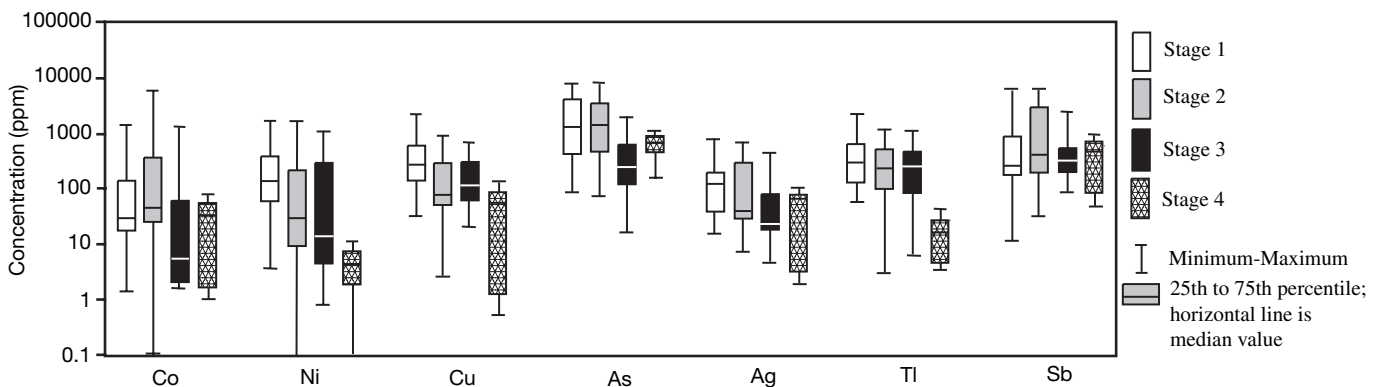


FIG. 9. Boxplots showing ranges of selected trace element concentrations in pyrite from stages 1 through 4 determined by LA-ICP-MS.

TABLE 2. Basic Statistics for Trace Element Contents in Pyrite from the Red Dog Deposits

	Min	Mean	Median	25 th	75 th	Max	% above MDL
Stage 1: Pyrite associated with early brown sphalerite, <i>n</i> = 49, deposits M, A							
Ag ppm	20	198	116	42	223	900	100
As	121	1,430	1,070	497	1,450	10,750	100
Co	2	138	41	22	103	1,420	100
Cu	41	438	300	156	638	2,160	100
Hg	1.3	9	6	4	10	63	94
Ni	6	315	185	71	482	1,660	98
Pb	1	13,230	1,770	274	2,720	170,660	100
Sb	7	908	421	204	925	6,720	100
Se	0.05	84	18	14	94	358	14
Tl	60	554	431	130	756	2,330	100
Zn	30	11,990	462	83	9,380	208,400	100
Stage 2: Pyrite associated with yellow-brown sphalerite, <i>n</i> = 24, deposits Q, M, A, P							
Ag ppm	8	206	58	31	763	800	100
As	24	2,600	1,370	481	4,040	8,990	100
Co	0.1	491	60	29	371	5,580	100
Cu	3	227	90	63	323	934	100
Hg	0.2	3	3	0.9	4.5	13	96
Ni	0.03	197	44	11	127	1,630	100
Pb	1	17,580	2,650	153	12,910	250,480	100
Sb	21	1,430	520	181	1,920	6,160	100
Se	0.05	19	18	9	26	46	21
Tl	2	436	366	100	597	12,220	100
Zn	3	5,690	2,530	310	10,570	23,470	100
Stage 3: Pyrite/marcasite associated with red-brown sphalerite, <i>n</i> = 20, deposits Q, M, A							
Ag ppm	6	80	30	18	98	480	100
As	16	551	372	126	793	1,960	100
Co	2	127	7	2.8	42	1,380	100
Cu	27	226	109	71	341	801	100
Hg	2	11	7	3	15	41	95
Ni	1	171	11	5	110	1,250	95
Pb	5	1,170	718	88	1,358	5,420	100
Sb	96	502	366	206	604	2,310	100
Se	3	58	45	11	61	181	30
Tl	7	400	273	87	542	1,170	100
Zn	22	18,290	409	177	3,525	192,010	100
Stage 4: Pyrite associated with late tan sphalerite, <i>n</i> = 9, deposit M							
Ag ppm	2	54	80	3	94	100	100
As	201	734	757	525	1,045	1,210	100
Co	1	33	45	1.6	59	80	100
Cu	0.7	57	73	1.3	103	136	100
Hg	0.2	3	3	2	3.6	4	100
Ni	0.03	6	5	2	9	14	100
Pb	2	1,170	516	88	1,360	5,420	100
Sb	49	415	613	77	653	820	100
Se	NA	NA	NA	NA	NA	NA	0
Tl	4	19	16	5	33	41	100
Zn	1	108	76	21	199	318	100

A = Aqqaluk, M = Main, Max = maximum value, MDL = minimum detection limits, Min = minimum value, NA = not applicable, P = Paalaaq, Q = Qanaiyaq, 25th = 25th percentile, 75th = 75th percentile

Values for MDL vary, but maximum MDL for this data set are as follows: Ag = 0.05, As = 0.05, Co = 0.5, Cu = 0.5, Hg = 0.1, Ni = 0.01, Pb = 0.5, Sb = 0.5, Se = 0.05, Tl = 0.05, Zn = 0.5

Discussion

Depositional environment

Although the simple mineralogy of stage 1 is similar to that of many sediment-hosted Zn-Pb deposits worldwide (Goodfellow et al., 1993, Lydon, 1995; Large et al., 2002), the textures

are unlike those believed to have formed by exhalative processes. Delicate monomineralic bands of sulfide and shale that characterize deposits such as Sullivan (Lydon et al., 2000), Rammelsberg (Large and Walcher, 1999), and McArthur River (Large et al., 2002) are rare at Red Dog. However, Red Dog textures are consistent with formation of

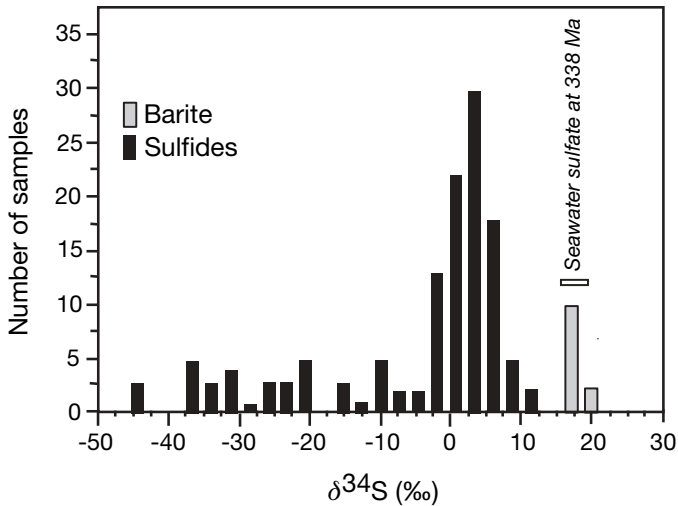


FIG. 10. Frequency distribution of sulfur isotope values for sulfides and ore-associated barite from the Red Dog deposits. Sulfide data were obtained by in situ analysis using ion microprobe techniques (Appendix). Barite sulfur isotope data by conventional analysis from Johnson et al. (2004).

sulfides near the sea floor during sedimentation. The fine-grained nature of stage 1 minerals suggests rapid coprecipitation that likely occurred from the mixing of seawater with ascending metalliferous fluids. Modern massive sulfide systems contain material that is largely in the 10 μm to 1 mm range (Herzig and Hannington, 1995). Colloform and dendritic textures and the spatial and temporal association with fine-grained barite are also common at modern sea-floor vents, such as at sediment-covered ridge axes (e.g., Koski and others, 1988; Goodfellow and Zierenberg, 1999). The simple mineralogy of stage 1 at Red Dog is similar to that of sulfide deposits at sediment-covered ridges, although the latter typically contain minor amounts of arsenopyrite, tetrahedrite, loellingite, and boulangerite, with barite, anhydrite, and amorphous silica in addition to Pb and Zn sulfides (Koski et al., 1988; Ames et al., 1993).

The abundance of barite at Red Dog might also be compared with that currently forming at cold seeps along modern continental margins. Sediment-free build-ups (up to 10 m thick) of irregular masses and layers of barite and minor pyrite in the Sea of Okhotsk are interpreted to have formed above the sediment surface with growth of barite into the water column (Greiner et al., 2002). Dendritic and layered barite with textures similar to those present at the Red Dog deposits also have been described in the Gulf of Mexico (Fu et al., 1994) and at the Peruvian margin (Torres et al., 1996). A major difference between these seep sites and the Red Dog deposits is that the former lack base metal sulfide minerals. However, the Red Dog barite deposit is anomalous in that it is the only one in the district that is spatially associated with base metal sulfides. Other barite deposits of equivalent age in the district either lack base metal sulfides, or are physically (and perhaps temporally) separated from the sulfide orebody by unmineralized black shale or mudstone (e.g., Anarraaq). Significantly, sulfur and oxygen isotope compositions of sulfide-barren barite deposits in the district are consistent with an origin like that of modern cold seeps (Johnson et al., 2004).

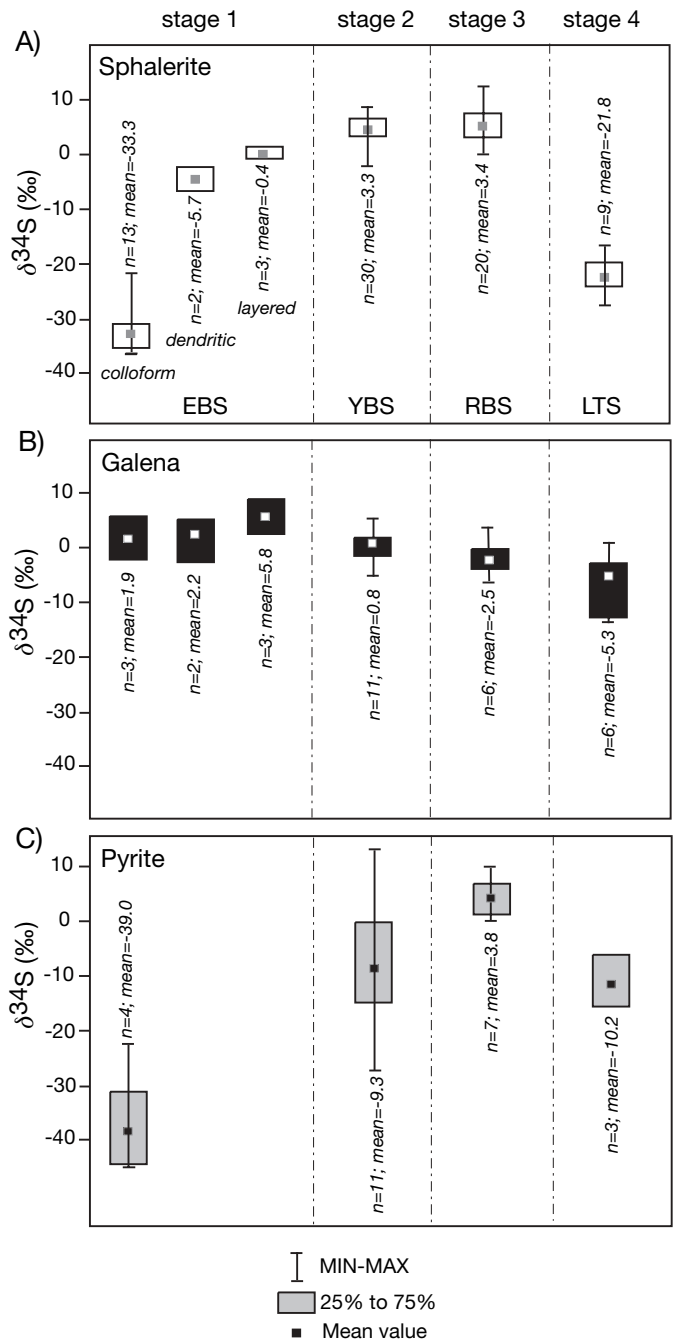


FIG. 11. Boxplots showing isotopic ranges of sphalerite, galena, and pyrite from stage 1 through 4 (data obtained by in situ analysis using ion microprobe techniques: Appendix). Number of samples for each stage or type and mean concentration is indicated next to each boxplot.

One possibility is that the barite at Red Dog formed in a similar cold-seep setting but was overprinted by a metal-bearing hydrothermal system.

Coarsening of barite in the Red Dog deposits was likely the consequence of hydrothermal recrystallization and overgrowth during introduction of stage 2 fluids from below. In large deposits in modern sea-floor settings (Herzig and Hannington, 1995) and some ancient examples (e.g., Eldridge et al., 1983), coarsening of mineral grains is a common result of

hydrothermal reworking. In this process, trace elements are also mobilized during interaction with upwelling hydrothermal fluids (Huston et al., 1995; Halbach et al., 2002). Although most commonly observed in volcanogenic massive sulfide deposits, subsurface-zone refinement caused by lateral and upward flow of hydrothermal fluids also has been suggested for some sediment-hosted sulfide deposits such as Sullivan (Lydon et al., 2000) and Middle Valley (Lydon et al., 1990; Goodfellow and Zierenberg, 1999).

The banding and crustification of stage 3 minerals in vein ore in the Red Dog deposits reflects deposition in open space. The common occurrence of multiple vein sets and the position of the veins primarily near the base and margins of the deposits have been suggested as evidence that the veins represent feeder zones to the massive sulfide mineralization (Moore et al., 1986; Young, 1989). However, yellow-brown sphalerite, the dominant type of sphalerite in massive sulfide ore, has not been observed in the veins. Thus, an alternative explanation is that the veins and associated breccias formed late in the mineralization history. Macroscopic textures of the Red Dog veins, such as multiple sets of high-angle planar veins and breccias with irregular and disoriented clasts of veined mudstone are similar to vein networks and hydraulic breccias that form in shallow levels of orogenic belts by hydrofracturing caused by pulses of high fluid pressure (Vanucchi and Maltman, 2000). The high fluid pressure that caused vein formation at Red Dog could have been the result of thermal alteration of organic-rich host rocks by the hydrothermal fluid and formation of volatile hydrocarbons (Nunn and Meulbroek, 2002; Warner, 1998).

Chemical conditions of sphalerite formation

Ore-stage sphalerites (stages 2 and 3) are geochemically similar (Fig. 8). Slight variations in Fe and other more subtle geochemical differences between yellow-brown and red-brown sphalerite most likely reflect increases in temperature or decreases in sulfur activity, or both (e.g., Scott, 1983; Vaughan and Craig, 1997). The pH, total sulfur content, and oxidation state of the fluid may also have influenced the abundances of trace elements in yellow-brown and red-brown sphalerite. Overall, the similarity in geochemical characteristics suggests that red-brown and yellow-brown sphalerite were deposited from a common fluid that experienced progressive or repetitive physicochemical changes.

Lower Fe contents and higher Tl and Mn contents in stage 1 early brown sphalerite relative to later yellow-brown and red-brown sphalerite (Fig. 8) are accompanied by variations in relative amounts of Zn, Pb, and Fe, as inferred from abundances of contemporaneous ore minerals. Stage 1 fluids were dominated by Zn (early brown sphalerite > pyrite > galena), whereas stage 2 and 3 fluids contained significantly more Pb and Fe. Although the source (or sources) of metals and precipitation mechanisms may have contributed to these differences, the fluid composition was probably a major control. Temperature may have been a factor, although data from modern metal-bearing brines show little to no correlation between temperature and metal concentration at temperatures below about 150°C (Hanor, 1997). Other factors, such as pH, the total concentration of sulfur, and oxidation state ($a_{\text{H}_2\text{S}}/a_{\text{SO}_4}$) were likely important (Cooke et al., 2000).

Analysis of modern brines and chemical modeling demonstrate that the highest Pb and Zn solubilities result from a combination of high salinity and low H_2S concentration (Hanor, 1997; Cooke et al., 2000). Salinities for stage 1 fluids are unknown. Redox conditions for the hydrothermal fluids can be qualitatively estimated using Mn contents of the sphalerite. Under reduced conditions, manganese is soluble and precipitation of Mn oxides is prohibited; Mn is readily incorporated into the sphalerite lattice as MnS (Vaughan and Craig, 1997). High Mn concentrations in sphalerite thus suggests relatively reduced conditions. Early brown sphalerite has higher Mn concentrations than yellow-brown and red-brown sphalerite (Fig. 9); therefore it is assumed that the fluids that deposited early brown sphalerite were relatively more reduced. Under these conditions, H_2S concentrations were probably higher than SO_4 , and the metal-carrying capacity of the early fluid was probably limited.

Sphalerite deposited in the late breccias (late tan sphalerite) contains significantly higher Mn and Tl, lower Fe and Co, and lower Cu/Ag ratios than all earlier stages. These compositional characteristics suggest that the sphalerite and other stage 4 sulfides precipitated from a reduced fluid that perhaps leached and remobilized elements from local preexisting sulfides.

Sources of sulfur and precipitation mechanisms

A plausible explanation for the isotopically low $\delta^{34}\text{S}$ values of early brown sphalerite and stage 1 pyrite is that reduced sulfur formed by bacterial reduction of sulfate from Carboniferous seawater. In this case, the $\delta^{34}\text{S}$ value of the colloform sphalerite would reflect a bacteriogenic fractionation of about 45 to 55 per mil. If the sulfur isotope compositions of dendritic and layered sphalerite do not include contamination from barite inclusions, the isotopic fractionation from seawater sulfate is smaller, on the order of about 15 to 25 per mil. Large ranges in fractionation are typical of bacterial reduction of sulfate in open or closed systems (Ohmoto and Goldhaber, 1997).

Bacterial reduction of sulfate typically occurs at temperatures of less than 60° to 80°C (Machel, 2001), although at some modern hydrothermal vent sites bacterial reduction of sulfate has been found to occur up to 110°C (Jorgensen et al., 1992). The rate and amount of H_2S that can be generated by bacterial reduction of sulfate increase if the availability of organic reactants and sulfate is high (Machel, 2001). The abundant barite in the district suggests a large homogeneous reservoir of sulfate (i.e., seawater), and sedimentologic and geochemical data suggest that the basin in which early (stage 1) barite and sulfides precipitated was characterized by high productivity of organic matter (Dumoulin et al., 2004; Slack et al., 2004a). These conditions are ideal for the production of large amounts of H_2S by bacterial reduction of seawater sulfate. The availability of metals such as Fe, Pb, and Zn may sharply decrease the amount of H_2S owing to the low solubilities of metals in the presence of H_2S and the resulting precipitation of sulfides (Machel, 2001). However, the paucity of stage 1 sulfides suggests that the supply of metals (especially reactive Fe) was limited (Slack et al., 2004a), which may have contributed to the high concentrations of H_2S that was available in the pore fluids.

Temperatures of yellow-brown and red-brown sphalerite were 100° to 200°C (Leach et al., 2004), and therefore some reduced sulfur could have been produced by thermochemical sulfate reduction (Machel, 2001). The fractionation between yellow-brown or red-brown sphalerite and most barite at Red Dog is about 15 per mil, which is typical for thermochemical sulfate reduction (Ohmoto and Goldhaber, 1997). Rates of thermochemical sulfate reduction are not well constrained, but experimental data (Goldhaber and Orr, 1995) suggest that in the presence of high initial concentrations of H₂S, rates are about 10⁻⁹ mol/l/year at 100°C, increasing three orders of magnitude at 150°C. This could have supplied significant H₂S during stages 2 and 3, with sulfate most likely derived from seawater or pore waters, and/or from reductive dissolution of preexisting barite (Johnson et al., 2004). Sulfate reduction and sulfide precipitation probably took place at the same site, but some H₂S likely migrated to the site of deposition.

The last stage of breccia formation and mineralization at Red Dog is characterized by low $\delta^{34}\text{S}$ values for all sulfides (mean $\delta^{34}\text{S}$ is -21.8‰ for late tan sphalerite; -5.3‰ for galena, and -10.2‰ for pyrite), suggesting derivation of H₂S by bacterial reduction of sulfate. Biogenic sulfur was likely produced during the 100 million years of sedimentation between stage 3 and 4.

The order of $\delta^{34}\text{S}$ values of pyrite, sphalerite, and galena in stages 1 and 4 (Fig. 11) indicates that the sulfides were precipitated out of isotopic equilibrium, most likely because of rapid precipitation rates or low temperatures (Ohmoto and Goldhaber, 1997). In contrast, $\delta^{34}\text{S}$ values for stage 2 and 3 sphalerite and galena follow expected patterns (i.e., values for sphalerite higher than galena), suggesting that isotopic equilibrium was achieved during precipitation. At the likely highest temperature for stages 2 and 3 (ca. 200°C; Leach et al., 2004), the isotopic difference between sphalerite and galena should be about 3.3 per mil (Ohmoto and Goldhaber, 1997). Texturally intergrown stage 2 and 3 sphalerite and galena pairs have isotopic differences ranging from 1.9 to 3.4 per mil, suggesting at least partial equilibrium.

Summary of Mineralizing Events

The history of mineralization at Red Dog is partly obscured by the “zone refining” process during introduction of stage 2 fluids, by late silicification that overprinted the orebody and replaced much of the barite, and by postmineralization (Jurassic to Cretaceous) deformation and thrusting during the Brookian orogeny. Nevertheless, textural and compositional data for barite and sulfides provide important insights into the environment of deposition of the Red Dog deposits and suggest that the distribution of ore and gangue minerals in the Red Dog deposits did not result from a single mineralizing event but rather from a four-stage process.

Stage 1—Deposition of barite and sulfides in unconsolidated muds

Stage 1 mineralization produced complex intergrowths of fine-grained barite, sphalerite, minor pyrite, and rare galena that were deposited mainly as subsurface impregnations in unconsolidated organic-rich muds of the Ikalukrok unit (Fig. 12A). By analogy with modern and ancient systems, upflow of hydrothermal fluids in unconsolidated sediments likely

formed a diapir of fluid that completely permeated the subsurface (Lydon et al., 2000). Textures indicating exhalation of brines on the sea floor, such as monomineralic banding of sulfide and shale, are rare at Red Dog. Elsewhere in the district, paragenetic and textural studies suggest that barite and sulfides replaced carbonate (e.g., Anarraaq; Kelley et al., 2004). However, the Red Dog deposits contain only minor amounts of carbonate, and unequivocal evidence for replacement of carbonate by barite or sulfides has not been documented. Possible explanations for the scarcity of carbonate at Red Dog include a lack of original carbonate turbidite deposition, dissolution by acidic ore fluids, or complete replacement of carbonate by barite and/or sulfides.

On the basis of sulfur and oxygen isotope data for sulfide-barren barite in the Red Dog district, Johnson et al. (2004) suggest that the barite formed at sites that were generating Ba and methane. Thick accumulations of sediment-free massive, layered, and dendritic barite at some of these sites have a number of textural similarities to Red Dog barite. Colloform early brown sphalerite and pyrite that coprecipitated with barite have average $\delta^{34}\text{S}$ values of -33.3 and -39.0 per mil, respectively, suggesting that H₂S was produced by bacterial sulfate reduction.

The chemistry of early brown sphalerite is characterized by low Fe and high Mn contents. The high Mn likely indicates that the fluids were reduced, and it may be inferred that H₂S > SO₄ (cf. Cooke et al., 2000). Sulfide proportions provide information about the metal budget. Compared with later stages, the amount of sulfide deposited during stage 1 was minor, and sphalerite was more abundant than pyrite or galena (i.e., Zn > Fe > Pb). It is assumed that H₂S was available at the site of deposition during stage 1, and therefore the amount of sulfides deposited during stage 1 was probably controlled largely by the availability of metals. Although the metal sources are uncertain, they may have been derived in situ from the organic-rich muds of the Ikalukrok unit. If this interpretation is correct, the low abundances of pyrite can be explained by low amounts of reactive Fe in the mudstones, as inferred by Slack et al. (2004a). Furthermore, in a high H₂S environment like that which is assumed at the site of deposition for stage 1, any Fe present would immediately precipitate as pyrite, resulting in low Fe contents of sphalerite and other sulfides that coprecipitated with pyrite.

Textural observations indicate that the early mineralizing event occurred during sedimentation and prior to lithification of the mudstones in the late Meramecian, which roughly coincides with the cessation of carbonate turbidite deposition from adjacent carbonate platforms (Dumoulin et al., 2004).

Stage 2—Hydrothermal coarsening of barite and precipitation of sulfides

Stage 2 is defined as the early main ore stage at Red Dog. Any genetic model for stage 2 must account for the following characteristics: (1) variable sulfide grain sizes of 50 μm to 200 mm; (2) textures indicating alternating and overlapping deposition of yellow-brown sphalerite and barite; (3) an increase in the abundance of galena and pyrite compared with the stage 1 mineral assemblage; (4) significantly higher Fe and Co and lower Mn and Tl contents in yellow-brown sphalerite compared with early brown sphalerite; (5) higher temperatures of formation (100°–200°C); (6) higher $\delta^{34}\text{S}$ values (avg = 3.35‰)

for yellow-brown sphalerite compared with stage 1; and (7) a consistent vertical ore stratigraphy with massive sulfide at the base and coarse-grained, sulfide-bearing barite at the top (Fig. 12B).

Stage 2 coincided with the demise of carbonate platforms owing to tectonic subsidence (Dumoulin et al., 2004). Evidence for rifting includes the presence of minor alkaline mafic igneous rocks in Kivalina and Ikalukrok units that predate stage 2 sulfides (Fig. 12B). The timing of this igneous activity is constrained by a $^{40}\text{Ar}/^{39}\text{Ar}$ age of 344 ± 3 Ma on biotite from a mafic intrusion in the Aqqaluk deposit (Werdon, 1999), by field relationships that show the intrusion predates massive sulfide mineralization, and by a Re-Os isochron age of 338 ± 5.8 Ma for stage 2 and 3 pyrite (Morelli et al., 2004). Although the volume of exposed igneous rocks at Red Dog is minor, there is evidence of significant intrusive activity farther east at the Drenchwater deposit (ca. 140 km east of Red Dog). Biotite from three Drenchwater intrusions yielded ages of 335 ± 2 Ma, 336 ± 3 Ma and 337 ± 3 Ma (Werdon, 1999), which are broadly contemporaneous with mineralization. Whereas igneous activity may have provided heat that promoted hydrothermal fluid flow, rare gas contents of sphalerite fluid inclusions indicate little contribution of magmatic volatiles to the ore fluids (Leach et al., 2004).

In addition to having a higher temperature, stage 2 fluids may have been relatively more oxidized than stage 1 fluids ($\text{SO}_4 > \text{H}_2\text{S}$). Moore et al (1986) and Young (1989) suggested that the reservoir for the metal-bearing fluids was clastic rocks of the Kanayut Conglomerate and/or Noatak Sandstone that stratigraphically underlie the Kuna Fm (Fig. 3). Within the underlying clastic rocks, stratabound but discordant sulfide-rich veins and breccias contain banded sulfides that are similar in appearance to veins at Red Dog. Geochemical and isotopic similarities between these veins and Red Dog sulfide veins argue for a similar origin (Young, 1995; Kelley et al., 2000). Lead isotope compositions of sulfides also suggest regional-scale mixing of two reservoirs. Lead from isotopically evolved crustal rocks probably mixed with deeply circulating fluids that mobilized less radiogenic lead from underlying Devonian-Mississippian clastic rocks (Ayuso et al., 2004).

The Kanayut Conglomerate and Noatak Sandstone that stratigraphically underlie the Kuna Formation formed in a fluvial-deltaic environment (Nilsen and Moore, 1982). Local accumulations of ferric iron-bearing minerals in these clastic rocks indicate oxidized conditions (L. Chapman, writ. commun., 2003). These rock compositions most likely buffered the stage 2 fluids and provide independent evidence that these fluids were oxidized.

Abundant textural evidence indicates that stage 2 sulfide deposition overlapped with precipitation of coarse-grained barite. Together with isotopic compositions, the data suggest that preexisting barite was reductively dissolved and hydrothermally coarsened during stage 2 mineralization (Fig. 12B). Reductive dissolution of barite by microbially mediated reactions (bacterial reduction of sulfate) has been demonstrated at low temperatures or by abiotic reactions (thermochemical sulfate reduction) at elevated temperatures. The temperatures inferred for stage 2 sphalerite (100° – 200°C) are sufficient for thermochemical sulfate reduction. During barite dissolution, Ba^{2+} would be remobilized upward and

reprecipitated as barite when Ba-rich fluids encountered sulfate-stable conditions (Johnson et al., 2004). The process described above probably took place entirely in the subsurface.

Stage 3—Deposition of barite and sulfides in veins and replacement of preexisting barite

The onset of stage 3 was marked by hydrofracturing and vein formation. During initial stage 3 and previous stages, hydrothermal fluids probably thermally altered the organic-rich mudstones and generated petroleum and hydrocarbon gases (Simoneit, 1993; Warner, 1998). If the sediments were unlithified or partly lithified, and therefore relatively porous and permeable, as is assumed for stage 1 and 2 (Fig. 12A-B), pore fluid and gas pressures could have been readily dissipated (e.g., Nunn and Meulbroek, 2002). However, with continued lithification and/or silicification prior to and during stage 2 mineralization (Slack et al., 2004b), permeability would have progressively decreased, leading to overpressuring, hydrofracturing, and vein formation (e.g., Vannucchi and Maltman, 2000; Bons, 2001) that was focused beneath the orebodies (Fig. 12C). Barite, red-brown sphalerite, pyrite or marcasite, galena, and minor chalcedonic silica were deposited in the veins, concurrent with replacement of barite in veins, massive sulfide, and sulfide-bearing barite (Fig. 12C).

Chemical and isotopic data for stage 3 sulfides indicate the fluids were similar to stage 2 fluids. However, fluctuations in T, pH, and/or the activities of sulfur species affected the metal ratios and metal abundances through time, resulting in compositionally zoned red-brown sphalerite. The ore fluids continued to flow through the clastic aquifer underlying the shale and ascended to the site of sulfide deposition in the Kuna Formation (Fig. 12C).

Similar sulfur isotope compositions of red-brown and yellow-brown sphalerite indicate a common source of H_2S from the reductive dissolution of barite \pm pore-water sulfate. One distinctive textural feature of stage 3 is that sphalerite pervasively replaces barite whereas stage 2 sulfides do not. The implication is that physiochemical conditions were such that barite was relatively more soluble during stage 3. Solubility of barite increases as a function of increasing pressure and salinity and with decreasing temperature from 200° to 100°C (Rimstidt, 1997; Hanor, 2000). It is assumed that temperature, pressure, and salinity remained fairly constant from stage 2 to 3, but it is possible that owing to hydrofracturing and vein development at the onset of stage 3, the temperature-pressure regime changed such that greater amounts of barite were dissolved.

Stage 4—Late breccias and deposition of fine-grained silica and tan sphalerite

The shallow dips of the late breccias containing late tan sphalerite are similar to flat-lying thrust faults in the area, although a consistent spatial association of the breccias with faults has not been observed. Pyrite clasts are fractured and broken indicating brittle deformation, whereas galena is plastically deformed and smeared into fractures.

The sulfide textures are consistent with formation of the breccias by tectonic processes during the Jurassic-Cretaceous Brookian orogeny. This timing implies that hydrothermal activity ceased after stage 3 mineralization. Sedimentary

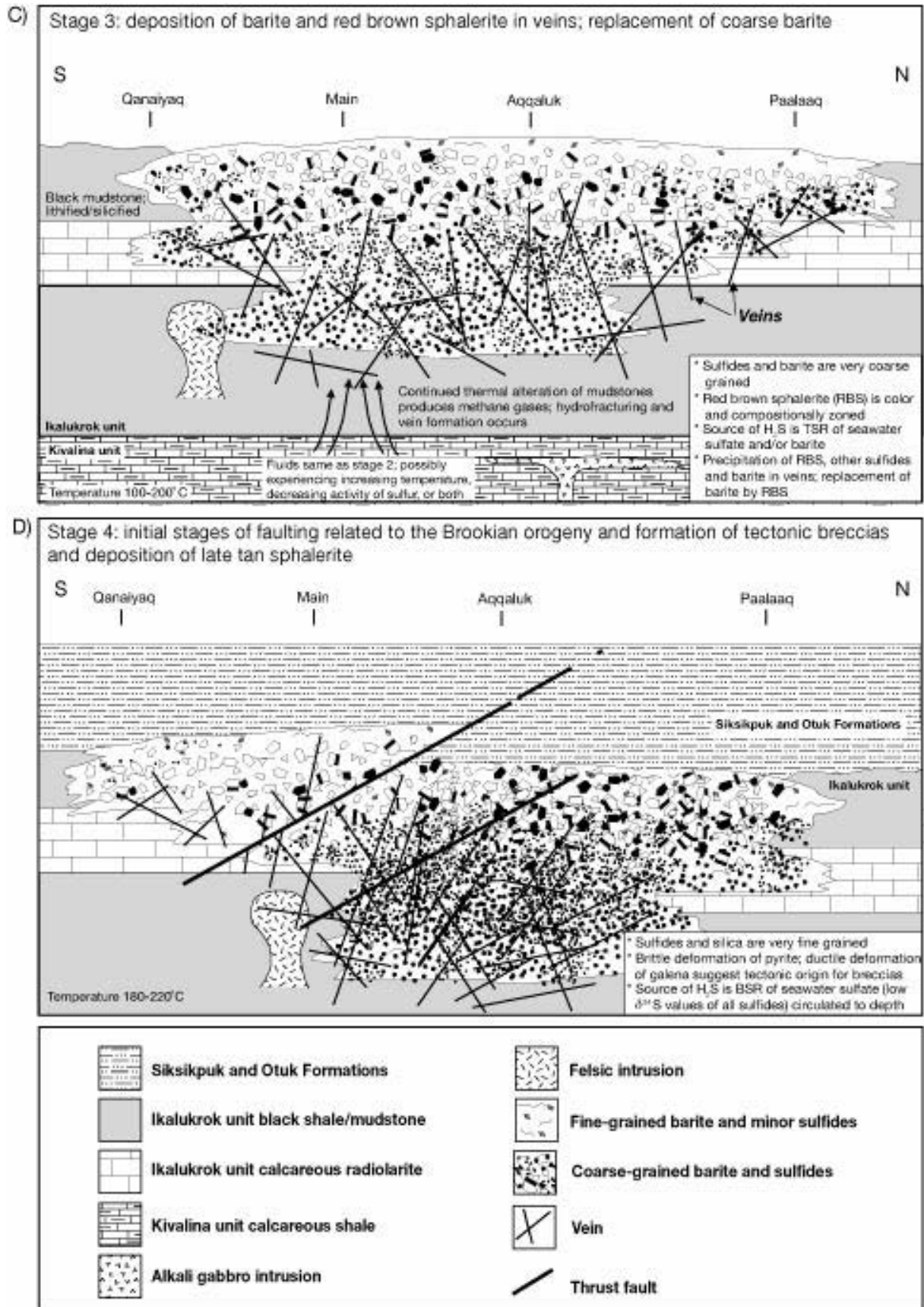


FIG. 12. (Cont.)

processes in Pennsylvanian-Triassic basins included formation of barite and local high organic matter production (Young, 2004). Biogenic H₂S that accumulated in pore water throughout the sedimentary section may have been circulated to depths during fluid flow related to the Brookian orogeny, thereby providing a source of sulfur for stage 4 sulfides. Pre-existing sulfides that were leached and remobilized by stage 4 fluids were a possible source of metals.

There is ample evidence that fluid flow during Mesozoic thrusting was widespread. On the basis of high formation pressures (500–3,400 bars) and temperatures (180°–220°C) in fluid inclusions, Leach et al. (2004) conclude that much of the quartz in and around the Red Dog deposits formed during Mesozoic thrusting. A similar Mesozoic timing was proposed for regionally widespread quartz-carbonate veinlets (Kelley et al., 2000). The texture of galena in the late breccias is also consistent with experimental results showing that at about 200°C and 500–2,000 bars, galena behaves plastically, displaying kink bands or curved cleavages (Salmon et al., 1974).

If the Brookian origin for the stage 4 breccias is correct, then the absence of these breccias in deposits other than Red Dog requires explanation. The simplest explanation is that Red Dog was the site of more focused, prolonged, and repeated hydrothermal fluid flow, not only in the Carboniferous but also later during Brookian time. Other deposits in the district not only lack stage 4-type breccias, but they also have markedly less abundant vein-type mineralization and less late (Brookian) quartz.

Conclusions

Throughout the Red Dog orebodies, four stages of sphalerite have distinct morphological, chemical, and isotopic characteristics. Evidence for exhalative processes is lacking, and unlike other deposits in the district, large-scale replacement of carbonate by barite or sulfides is not documented at the Red Dog deposits. Rather, the petrographic, geochemical, and isotopic data support a model in which early fine-grained barite and volumetrically minor sulfides formed at or near the sea floor in unconsolidated mud (stage 1). This stage was followed by subsea-floor zone refining and hydrothermal coarsening of barite caused by the introduction of ore-stage metal-rich fluids (stage 2). Metal-rich fluids reductively dissolved the preexisting barite to produce H₂S and induce sulfide mineral formation. With continued flow of hydrothermal fluids, progressive thermal alteration of organic-rich mudstones produced methane that led to fluid overpressuring, hydrofracturing, and vein formation (stage 3). Barite was pervasively replaced by sphalerite suggesting that barite solubility increased during stage 3. Hydrothermal activity ceased and sedimentary processes resumed until Jurassic time when thrusting and large-scale fluid flow related to the Jurassic to Cretaceous Brookian orogeny resulted in metal remobilization and formation of sphalerite-rich tectonic breccias. Abundant quartz formed during this event replaced some remaining barite and obscured primary textural features.

Acknowledgments

This work, a cooperative project between the U.S. Geological Survey and Teck Cominco, was initiated in 1998. We are grateful to all previous and current Teck Cominco staff

involved in the study. Specifically, we thank George Cole and Scott Jennings for their role in getting the research plan underway and, together with Adrian King, for scientific, logistic, and financial support throughout the project. Tom Krolak, Bob Robinson, Gary Coulter, and Lorne Young provided valuable background information that was critical for building the necessary framework for our studies. Cameron Rombach, Erin Marsh, and Erin Kelley helped with various aspects of report preparation including drafting, editing, and assembly. Technical reviews by Randy Koski and Peter McGoldrick greatly improved the manuscript.

REFERENCES

- Ames, D.E., Franklin, J.M., and Hannington, M.D., 1993, Mineralogy and geochemistry of active and inactive chimneys and massive sulfide, Middle Valley, northern Juan de Fuca Ridge; an evolving hydrothermal system: *Canadian Mineralogist*, v. 31, p. 997–1024.
- Ayuso, R.A., Kelley, K.D., Leach, D.L., Young, L.E., Slack, J.F., Wandless, G., Lyon, A.M., and Dillingham, J.L., 2004, Origin of the Red Dog Zn-Pb-Ag deposits, Brooks Range, Alaska: Evidence from regional Pb and Sr isotope sources: *ECONOMIC GEOLOGY*, v. 99, p. 1533–1553.
- Bons, P.D., 2001, The formation of large quartz veins by rapid ascent of fluids in mobile hydrofractures: *Tectonophysics*, v. 336, p. 1–17.
- Cooke, D.R., Bull, S.W., Large, R.R., and McGoldrick, P.J., 2000, The importance of oxidized brines for the formation of Australian Proterozoic stratiform sediment-hosted Pb-Zn (sedex) deposits: *ECONOMIC GEOLOGY*, v. 95, p. 1–18.
- Crowe, D.E., and Vaughan, R.G., 1996, Characterization and use of isotopically homogeneous standards for in situ laser microprobe analysis of ³⁴S/³²S ratios: *American Mineralogist*, v. 81, p. 187–193.
- Dumoulin, J.A., Harris, A.G., Blome, C.D., and Young, L.E., 2004, Depositional settings, correlation, and age of Carboniferous rocks in the western Brooks Range, Alaska: *ECONOMIC GEOLOGY*, v. 99, p. 1355–1384.
- Edgerton, D., 1997, Reconstruction of the Red Dog Zn-Pb-Ba orebody, Alaska: Implications for the vent environment during the mineralizing event: *Canadian Journal of Earth Sciences*, v. 34, p. 1581–1602.
- Eldridge, C.S., Barton, P.B., Jr., and Ohmoto, H., 1983, Mineral textures and their bearing on the formation of the Kuroko orebodies: *ECONOMIC GEOLOGY MONOGRAPH* 5, p. 241–281.
- Frisia, S., Borsato, A., Fairchild, I.J., and McDermott, F., 2000, Calcite fabrics, growth mechanisms, and environments of formation in speleothems from the Italian Alps and southwestern Ireland: *Journal of Sedimentary Research*, v. 70, p. 1183–1196.
- Fu, B., Aharon, P., Byerly, G.R., and Roberts, H.H., 1994, Barite chimneys on the Gulf of Mexico slope: Initial report on their petrography and geochemistry: *Geo-Marine Letters*, v. 14, p. 81–87.
- Goldhaber, M.B., and Orr, W.L., 1995, Kinetic controls on thermochemical sulfate reduction as a source of sedimentary H₂S: *American Chemical Society Symposium Series*, v. 612, p. 412–425.
- Goodfellow, W.D., and Zierenberg, R.A., 1999, Genesis of massive sulfide deposits at sediment-covered spreading centers: *Reviews in Economic Geology*, v. 8, p. 297–324.
- Goodfellow, W.D., Lydon, J.W., and Turner, R.J.W., 1993, Geology and genesis of stratiform sediment-hosted (sedex) zinc-lead-silver sulfide deposits: *Geological Association of Canada Special Paper* 40, p. 201–251.
- Greiner, J., Bollwerk, S.M., Derkacev, A., Bohrmann, G., and Suess, E., 2002, Massive barite deposits and carbonate mineralization in the Derugin basin, Sea of Okhotsk: Precipitation processes at cold seep sites: *Earth and Planetary Science Letters*, v. 203, p. 165–180.
- Halbach, M., Halbach, P., and Lüders, V., 2002, Sulfide-impregnated and pure silica precipitates of hydrothermal origin from the central Indian Ocean: *Chemical Geology*, v. 182, p. 357–375.
- Hanor, J.S., 1997, Controls on the solubilization of lead and zinc in basinal brines: *Society of Economic Geologists Special Publication* 4, p. 483–500.
- 2000, Barite-celestite geochemistry and environments of formation: *Reviews in Mineralogy and Geochemistry*, v. 40, p. 193–275.
- Harland, W.B., Armstrong, R.L., and others, 1990, *A geologic time scale 1989*: Cambridge, Cambridge University Press, 263 p.
- Herzig, P.M., and Hannington, M.D., 1995, Polymetallic massive sulfides at the modern seafloor: A review: *Ore Geology Reviews*, v. 10, p. 95–115.

- Huston, D.L., Sie, S.H., Suter, G.F., Cooke, D.R., and Both, R.A., 1995, Trace elements in sulfide minerals from eastern Australian volcanic-hosted massive sulfide deposits: Part I. Proton microprobe analyses of pyrite, chalcopyrite, and sphalerite, and Part II. Selenium levels in pyrite: Comparison with $\delta^{34}\text{S}$ values and implications for the source of sulfur in volcanogenic hydrothermal systems: *ECONOMIC GEOLOGY*, v. 90, p. 1167–1196.
- Jennings, S., and King, A.R., 2002, Geology, exploration history and future discoveries in the Red Dog district, western Brooks Range, Alaska: Centre for Ore Deposit Research Special Publication 4, p. 151–158.
- Jiuling, Li, 1993, The Tl-Zn-S and Tl-Cd-S systems in comparison with the Tl-Hg-S system: *Neues Jahrbuch Miner. Abh.*, v. 166, p. 53–58.
- Johnson, C.A., Kelley, K.D., and Leach, D.L., 2004, Sulfur and oxygen isotopes in barite deposits of the western Brooks Range, Alaska, and implications for the origin of the Red Dog massive sulfide deposits: *ECONOMIC GEOLOGY*, v. 99, p. 1435–1448.
- Jorgensen, B.B., Isaksen, M.F., Jannasch, H.W., 1992, Bacterial sulfate reduction above 100°C in deep-sea hydrothermal vent sediments: *Science*, v. 258, p. 1756–1757.
- Kelley, K.D., Leach, D.L., and Johnson, C.A., 2000, Sulfur-, oxygen-, and carbon-isotope studies of Ag-Pb-Zn vein-breccia occurrences, sulfide-bearing concretions, and barite deposits in the north-central Brooks Range, with comparisons to shale-hosted stratiform massive sulfide deposits: U.S. Geological Survey Professional Paper 1615, p. 189–201.
- Kelley, K.D., Dumoulin, J.A., and Jennings, S., 2004, The Anarraaq Zn-Pb-Ag and barite deposit, northern Alaska: Evidence for replacement of carbonate by barite and sulfides: *ECONOMIC GEOLOGY*, v. 99, p. 1577–1591.
- Koski, R.A., Shanks, W.C. III., Bohrsen, W.A., and Oscarson, R.L., 1988, The composition of massive sulfide deposits from the sediment-covered floor of Escanaba trough, Gorda Ridge: Implications for depositional processes: *Canadian Mineralogist*, v. 26, p. 655–673.
- Large, D.E., and Walcher, E., 1999, The Rammelsberg massive sulfide Cu-Zn-Pb-Ba deposit, Germany: An example of sediment-hosted, massive sulfide mineralization: *Mineralium Deposita*, v. 34, p. 522–538.
- Large, R.R., Bull, S.W., Selley, D., Yang, J., Cooke, D., Garven, G., and McGoldrick, P., 2002, Northern Australian Proterozoic sediment-hosted Zn-Pb-Ag deposits: A summary: Centre for Ore Deposit Research Special Publication 4, p. 159–160.
- Leach, D.L., Marsh, E., Emsbo, P., Rombach, C., Kelley, K.D., and Anthony, M., 2004, Nature of hydrothermal fluids at the shale-hosted Red Dog Zn-Pb-Ag deposits, Brooks Range, Alaska: *ECONOMIC GEOLOGY*, v. 99, p. 1449–1480.
- Leshin, L.A., McKeegan, K.D., Carpenter, P.K., and Harvey, R.P., 1998, Oxygen isotopic constraints on the genesis of carbonates from Martian meteorite ALH84001: *Geochimica Cosmochimica Acta*, v. 62, p. 3–13.
- Leventhal, J.S., Johnson, C.A., and Kelley, K.D., 2002, Isotopic and geochemical constraints for witherite (BaCO_3) from the sediment-hosted Zn-Pb-Ag massive sulfide deposits, Red Dog district, Alaska [abs.]: Geological Society of America Abstracts with Programs, v. 34, p. 220.
- Lydon, J.W., 1995, Sedimentary exhalative sulphides (sedex): Geological Survey of Canada—Geology of Canada 8, p. 130–152.
- Lydon, J.W., Goodfellow, W.D., and Franklin, J.M., 1990, Chemistry of sediment pore waters around active hydrothermal vents, Middle Valley [abs.]: EOS, Transactions American Geophysical Union, v. 71, p. 1569.
- Lydon, J.W., Paakki, J.J., Anderson, H.E., and Reardon, N.C., 2000, Overview of the geology and geochemistry of the Sullivan deposit: Geological Association of Canada Special Publication 1, p. 505–522.
- Machel, H.G., 2001, Bacterial and thermochemical sulfate reduction in diagenetic settings—Old and new insights: *Sedimentary Geology*, v. 140, p. 143–175.
- Marshall, B., Vokes, F.M., and Larocque, A.C.L., 2000, Regional metamorphic remobilization: Upgrading and formation of ore deposits: Reviews in *ECONOMIC GEOLOGY*, v. 11, p. 19–38.
- Mayfield, C.F., Tailleux, I.L., and Ellersieck, Inyo, 1988, Stratigraphy, structure, and palinspastic synthesis of the western Brooks Range, northwestern Alaska: U.S. Geological Survey Professional Paper 1399, p. 143–186.
- McKibben, M.A., and Riciputi, L.R., 1998, Sulfur isotopes by ion microprobe: Reviews in *ECONOMIC GEOLOGY*, v. 7, p. 121–139.
- Moore, D.W., Young, L.E., Modene, J.S., and Plahuta, J.T., 1986, Geologic setting and genesis of the Red Dog zinc-lead-silver deposit, western Brooks Range, Alaska: *ECONOMIC GEOLOGY*, v. 81, p. 1696–1727.
- Moore, T.E., Wallace, W.K., Bird, K.J., Karl, S.M., Mull, C.G., and Dillon, J.T., 1994, Geology of northern Alaska: Geological Society of America—The geology of North America, v. G-1, p. 49–140.
- Morelli, R.M., Creaser, R.A., Selby, D., Kelley, K.D., Leach, D.L., and King, A.R., 2004, Re-Os sulfide geochronology of the Red Dog sediment-hosted Zn-Pb-Ag deposits, Brooks Range, Alaska: *ECONOMIC GEOLOGY*, v. 99, p. 1569–1576.
- Mull, C.G., 1982, The tectonic evolution and structural style of the Brooks Range, Alaska—An illustrated summary, in Powers, R.B., ed., Geological studies of the Cordilleran thrust belt: Rocky Mountain Association of Geologists, v. 1, p. 1–45.
- Mull, C.G., and Werdon, M.B., 1994, Generalized geologic map of the western Endicott Mountains, central Brooks Range, Alaska: Alaska Division of Geological and Geophysical Surveys Public Data File 94-55, 1 sheet, scale 1:250,000.
- Mull, C.G., Tailleux, I.L., Mayfield, C.F., Ellersieck, Inyo, and Curtis, Steve, 1982, New upper Paleozoic and lower Mesozoic stratigraphic units, central and western Brooks Range, Alaska: American Association of Petroleum Geologists Bulletin, v. 66, no. 7, p. 348–362.
- Naslund, H.R., 1984, Supersaturation and crystal growth in the roof-zone of the Skaergaard magma chamber: Contributions to Mineralogy and Petrology, v. 86, p. 89–93.
- Nilsen, T.H., and Moore, T.E., 1982, Sedimentology and stratigraphy of the Kanayut Conglomerate, central and western Brooks Range, Alaska: U.S. Geological Survey Open File Report 82-0674, 68 p.
- Norman, M., Robinson, P., and Clark, D., 2003, Major- and trace-element analysis of sulfide ores by laser-ablation ICP-MS, solution ICP-MS, and XRF: New data on international reference materials: *Canadian Mineralogist*, v. 41, p. 293–305.
- Nunn, J.A., and Meulbroek, P., 2002, Kilometer-scale upward migration of hydrocarbons in geopressured sediments by buoyancy-driven propagation of methane-filled fractures: American Association of Petroleum Geologists Bulletin, v. 86, p. 907–918.
- Ohmoto, H., and Goldhaber, M.B., 1997, Sulfur and carbon isotopes, in Barnes, H.L., ed., Geochemistry of hydrothermal ore deposits—third edition: New York, John Wiley, p. 517–612.
- Riciputi, L.R., 1996, A comparison of extreme energy filtering and high mass resolution techniques for the measurement of $^{34}\text{S}/^{32}\text{S}$ ratio by ion microprobe: *Rapid Communications in Mass Spectrometry*, v. 10, p. 282–286.
- Riciputi, L.R., Paterson, B.A., and Ripperdan, R.L., 1998, Measurement of light stable isotope ratios by SIMS: Matrix effects for oxygen, carbon, and sulfur isotopes in minerals: *International Journal of Mass Spectrometry*, v. 178, p. 81–112.
- Ridley, W.I., 2000, The ICP-MS laser microprobe: A new geochemical tool: Trends in Geochemistry, v. 1, p. 1–14.
- Ridley, W.I., and Lichte, F.E., 1998, Major, trace, and ultratrace element analysis by laser ablation ICP-MS: Reviews in *Economic Geology*, v. 7, p. 199–215.
- Rimstidt, J.D., 1977, Gangue mineral transport and deposition, in Barnes, H.L., ed., Geochemistry of hydrothermal ore deposits—third edition: New York, John Wiley, p. 487–515.
- Rombach, C.S., and Layer, P.W., 2004, Geochronology of the western and central Brooks Range: Implications for the geologic evolution of the Anarraaq and Red Dog Zn-Pb-Ag deposits: *ECONOMIC GEOLOGY*, v. 99, p. 1307–1322.
- Salmon, B.C., Clark, C.R., and Kelly, W.C., 1974, Sulfide deformation studies: II. Experimental deformation of galena to 2,000 bars and 400°C: *ECONOMIC GEOLOGY*, v. 69, p. 1–16.
- Schmidt, J.M., and Zierenberg, R.A., 1988, Reconstruction of primary features and isotopic evidence for multiple sulfur sources at the Red Dog zinc-lead-silver deposit, Noatak district, Alaska: U.S. Geological Survey Circular 1035, p. 62–63.
- Scott, S.D., 1983, Chemical behavior of sphalerite and arsenopyrite in hydrothermal and metamorphic environments: *Mineralogical Magazine*, v. 47, p. 427–435.
- Shimizu, N., and Hart, S.R., 1982, Applications of the ion microprobe to geochemistry and cosmochemistry: Annual Review of Earth and Planetary Sciences, v. 10, p. 483–526.
- Simoneit, B.R.T., 1993, Hydrothermal alteration of organic matter in marine and terrestrial systems, in Engel, M.H., and Macko, S.A., eds., Organic geochemistry: Principles and applications: New York, Plenum Press, p. 397–418.
- Sims, D.B., 1996, The relationships of ore and structural geology at the Red Dog zinc-lead-silver deposit, western Brooks Range, Alaska: Unpublished Ph.D. dissertation, Tucson, Arizona, University of Arizona, 142 p.

- Slack, J.F., Dumoulin, J.A., Schmidt, J.M., Young, L.E., and Rombach, C.S., 2004a, Paleozoic sedimentary rocks in the Red Dog Zn-Pb-Ag district and vicinity, western Brooks Range, Alaska: Provenance, deposition, and metallogenic significance: *ECONOMIC GEOLOGY*, v. 99, p. 1385–1414.
- Slack, J.F., Kelley, K.D., Anderson, V.M., Clark, J.L., and Ayuso, R.A., 2004b, Multistage silicification and Fe-Tl-As-Sb-Ge-REE enrichment in the Red Dog Zn-Pb-Ag district, northern Alaska: Geochemistry, origin, and exploration applications: *ECONOMIC GEOLOGY*, v. 99, p. 1481–1508.
- Torres, M.E., Bohrmann, G., Suess, E., 1996, Authigenic barites and fluxes of barium associated with fluid seeps in the Peru subduction zone: *Earth and Planetary Science Letters*, v. 144, p. 469–481.
- Valley, J.W., and Graham, C.M., 1991, Ion microprobe analyses of oxygen isotopes in magnetite and ilmenite [abs.]: *Eos, Transactions, American Geophysical Union*, v. 72, p. 17, 292.
- Valley, J.W., Eiler, J.M., Graham, C.M., Gibson, E.K., Jr., and Romanek, C.S., 1997, Ion microprobe analysis of oxygen and carbon isotope ratios in the ALH84001 [abs.]: *Lunar and Planetary Science Conference*, v. 28, p. 1475–1476.
- Vannucchi, P., and Maltman, A.J., 2000, Insights into shallow-level processes of mountain building from the northern Apennines, Italy: *Geological Society of London Journal*, v. 157, p. 105–120.
- Vaughan, D.J., and Craig, J.R., 1997, Sulfide mineral stabilities, morphologies, and intergrowth textures, in Barnes, H.L., ed., *Geochemistry of hydrothermal ore deposits—third edition*: New York, John Wiley, p. 367–434.
- Warner, M.C., 1998, Geochemical characterization of sedimentary organic matter and hydrothermal petroleum in the black-shale-hosted Zn-Pb deposit at Red Dog mine, western Brooks Range, Alaska: Unpublished Ph.D. thesis, Bloomington, Indiana University, 216 p.
- Werdon, M.B., 1996, Drenchwater, Alaska: Zn-Pb-Ag mineralization in a mixed black shale-volcanic environment, in Coyner, A.R., and Fahey, P.L., eds., *Geology and ore deposits of the American Cordillera: Geological Society of Nevada Symposium, Reno/Sparks, Nevada, April 1995, Proceedings*, p. 1341–1354.
- 1999, *Geology and timing of Zn-Pb-Ag mineralization, northern Brooks Range, Alaska*: Unpublished Ph.D. dissertation, Fairbanks, University of Alaska, 130 p.
- Williams, G.E., 1979, Sedimentology, stable-isotope geochemistry and paleo-environment of dolostones capping late Precambrian glacial sequences in Australia: *Journal of the Geological Society of Australia*, v. 26, p. 377–386.
- Wilson, S.A., Ridley, W.I., and Koenig, A.E., 2002, Development of sulfide calibration standards for the laser ablation inductively-coupled plasma mass spectrometry technique: *Journal of Analytical Atomic Spectrometry*, v. 17, p. 406–409.
- Young, L.E., 1989, *Geology and genesis of the Red Dog deposit, western Brooks Range, Alaska*: Canadian Institute of Mining and Metallurgy Bulletin, v. 82, p. 57–67.
- 1995, Empirical applications of common lead-isotope ratios to exploration: *Society of Economic Geologists Newsletter*, no. 22, p. 7–12.
- 2004, A geologic framework for mineralization in the western Brooks Range, Alaska: *ECONOMIC GEOLOGY*, v. 99, p. 1281–1306.
- Yu, M.L., and Lang, N., 1986, Mechanisms of atomic ion emission during sputtering: *Nuclear Instruments and Methods in Physics Research*, v. 14, p. 403–413.
- Zierenberg, R.A., and Schmidt, J.M., 1988, Isotopic evidence for multiple sulfur sources at the Red Dog Zn-Pb-Ag deposit, Noatak district, Alaska [abs.]: *Geological Society of America Abstracts with Programs*, v. 20, p. A-37.

